Spectral Induced Polarization imaging to monitor seasonal and annual dynamics of frozen ground at a mountain permafrost site in the Italian Alps

Theresa Maierhofer[1,2], Adrian Flores Orozco[1], Nathalie Roser[1], Jonas K. Limbrock[4], Christin Hilbich[2], Clemens Moser[1], Andreas Kemna[4], Elisabetta Drigo[5], Umberto Morra di Cella[3], Christian Hauck[2]

[1]Department of Geodesy and Geoinformation, TU-Wien, Vienna, 1040, Austria
[2]Department of Geosciences, University of Fribourg, Fribourg, 1700, Switzerland
[3]Environmental Protection Agency of Aosta Valley (ARPA), Saint-Christophe, 11020, Italy
[4]Institute of Geosciences, Geophysics Section, University of Bonn, Bonn, 53115, Germany
[5]Geologist freelance, Aosta valley, Saint-Pierre, 11010, Italy

Correspondence to: Theresa Maierhofer (theresa.maierhofer@tuwien.ac.at)

Abstract. We investigate the application of spectral induced polarization (SIP) monitoring to understand seasonal and annual variations of freeze-thaw processes in permafrost, by examining the frequency dependence of subsurface electrical properties. We installed a permanent SIP monitoring profile at a high mountain permafrost site in the Italian Alps in 2019 and collected SIP data in the frequency range between 0.1-75 Hz over 3 years. The SIP imaging results were interpreted in conjunction with complementary seismic and borehole datasets. In particular, we investigated the phase frequency effect (ϕFE), i.e., the change of resistivity phase with frequency. We observe that this parameter (ϕFE) is strongly sensitive to temperature changes and might be used as a proxy to delineate spatial and temporal changes of ice content in the subsurface, providing information not accessible through electrical resistivity tomography (ERT) or single-frequency IP measurements. Temporal changes in ϕFE are validated through laboratory SIP measurements on samples from the site in controlled freeze-thaw experiments. We demonstrate that SIP is capable of resolving temporal changes in the thermal state and the ice/water ratio associated with seasonal freeze-thaw processes. We investigate the consistency between the ϕFE observed in field data, and ground water and ice content estimates derived from petrophysical modelling of ERT and seismic data.

1 Introduction

High-mountain environments are facing a rapid increase in air temperatures due to the amplification of the warming rate with elevation (Pepin et al., 2015), accelerating the rate of change of mountain permafrost systems and leading to increased permafrost temperatures, active layer (AL) thickening and decreasing ice contents (e.g., Biskaborn et al., 2019; Etzelmüller et al. 2020; Smith et al., 2022; Wu and Zhang, 2010). The change in the thermal state of the subsurface impacts slope stability (e.g., Ravanel et al., 2017) and water storage capacities (e.g. Harrington et al., 2018; Hilbich et al., 2022; Mathys et al., 2022; Rangecroft et al., 2016) making continuous temperature monitoring of the permafrost evolution in mountainous regions more

and more important, i.e. as part of global (Global Terrestrial Network of Permafrost, GTNP), continental (Permafrost and Climate in Europe, PACE project) and regional (such as the Swiss Permafrost Monitoring Network) monitoring programmes (e.g., Biskaborn et al., 2015; Harris et al., 2001; PERMOS, 2021).

Electrical resistivity tomography (ERT) is known to provide high-resolution spatial estimates about subsurface electrical properties sensitive to variations in temperature and water content, complementing spatially sparse borehole monitoring observations (e.g., Hauck, 2002; Hauck et al., 2013; Krautblatter et al., 2010; Oldenborger and LeBlanc 2018; Parkhomenko, 1982). Hence, in the last decades electrical monitoring arrays were set up at several permafrost sites throughout different European mountain ranges to assess the temporal evolution of subsurface properties and processes relevant for permafrost investigations (e.g., Etzelmüller et al. 2020; Hauck, 2002; Hilbich et al, 2008; Isaksen et al., 2011; Keuschnig et al. 2017; Krautblatter & Hauck, 2007; Mollaret et al., 2019; Pogliotti et al., 2014; Supper et al., 2014). In unfrozen conditions, comparatively low resistivity values are observed due to electrolytic conduction taking place within the interconnected pore-space and along the electrical double layer (EDL) formed at the interface between water and mineral surfaces (e.g., Revil and Glover, 1998; Ward, 1990; Waxman and Smits, 1968). Below the freezing point, the mobility of the ions is reduced, and part of the liquid pore water is transformed into ice leading to an exponential increase of the electrical resistivity with decreasing temperatures (e.g., Hauck, 2002; Oldenborger and LeBlanc, 2018, Oldenborger, 2021). Additionally, repeated electrical resistivity surveys were used to estimate relative changes in unfrozen water content (UWC) (Hauck, 2002; Hilbich et al., 2008; Oldenborger and LeBlanc, 2018), that is the fraction of water remaining unfrozen below the freezing point even at relatively low temperatures.

Nonetheless, the interpretation of electrical signatures in terms of ice, air and rock are still open to discussion and uncertainties remain (Hauck and Kneisel, 2008) that are often reduced by combining ERT investigations with complementary geophysical methods such as Refraction Seismic Tomography (RST) due to its sensitivity to changes in mechanical properties between unfrozen and frozen materials (e.g., Hausmann et al., 2007; Hilbich, 2010; Mollaret et al., 2020; Steiner et al., 2021). Seismic and electrical data sets were combined in various studies to estimate volumetric ice, water and air contents using the so-called 4-phase model (4PM) approach (by Hauck et al., 2011). The 4PM has been implemented in a petrophysical joint inversion (PJI) framework for a simultaneous inversion of geophysical datasets (Wagner et al., 2019). However, the presence of ice and the electrical double layer (EDL) formed at the water-ice interface requires the consideration of surface conduction (e.g., Bullemer and Riehl 1966; Carantl and Illlngworth 1982) which has not yet been implemented in the PJI.

To account for surface conduction, the induced polarization (IP), also known as complex resistivity method has been tested for permafrost applications (e.g., Doetsch et al., 2015; Bazin et al., 2019; Duvillard et al., 2018, 2021). Expressed in terms of the complex resistivity, the real component relates to the resistivity measured through ERT, while the imaginary component relates to surface conductivity arising e.g. from the accumulation and polarization of charges at the EDL formed in the ice-water or rock-water interface as well as protonic defects in ice surface. While IP measurements are typically collected in a frequency range between 0.1 to 1000 Hz (in the so-called spectral IP, SIP) (Lesmes and Frye, 2001), the measurement of the

full ice relaxation process requires the use of the high-frequency IP (HFIP) with frequencies up to 100 kHz. HFIP field measurements (Przyklenk et al., 2016) have revealed an improved delineation of the ground ice content as shown in Mudler et al. (2022). The enhanced polarization response at high frequencies is due to the motion of charge defects in the hydrogen-bonded ice lattice dominant at frequencies between 4 and 11 kHz for pure ice (Auty and Cole, 1952). The collection of high-frequency IP data remains challenging due to electromagnetic coupling effects, e.g., arising due to current leakage associated to the high impedance of soil, electrodes and cables (e.g., Binley et al. 2005; Flores Orozco et al., 2018; Ingeman-Nielsen, 2006; Kemna et al. 2012; Wang and Slater, 2019; Zimmerman et al., 2008). For lower frequencies, Kemna et al. (2014a) and Revil et al. (2019) attributed the SIP freezing/thawing behaviour in saturated rocks to both residual water films (bound water) at the ice and mineral surfaces, as well as the presence of water in smaller pores with a sufficiently reduced melting point as governed by the Gibbs-Thomson effect.

Duvillard et al. (2021) applied a petrophysical model calibrated through laboratory data to quantify the temperature distribution of a permafrost-affected rock ridge from time-domain IP data. Mudler et al. (2022) estimated the ice content obtained from broadband SIP inversion results conducted at a permafrost site in Siberia. Grimm and Stillman (2015) found temperature-dependent relationships between the ice volume fraction and the resistivity frequency effect (RFE) (see e.g. Vinegar and Waxman, 1984) in the laboratory and were able to estimate ice volumes at a frozen silt permafrost site. Maierhofer et al. (2022) showed that SIP data reduce the ambiguity in the interpretation of electrical resistivity data in a talus slope, a typical mountain permafrost landform consisting of coarse blocks and heterogeneously distributed ground ice contents. They show that ice-rich blocky material, unfrozen coarse blocky environments and bedrock (unfrozen and frozen) can result in similarly high resistivity values, but can be distinguished by distinct IP responses. Moreover, they demonstrate that ice-rich areas are associated with a significant increase in the IP response for data collected above 10 Hz, as also reported by Grimm and Stillman (2015).

Laboratory studies have investigated SIP responses in a frequency range between 0.01 Hz and 40 kHz during freezing/thawing periods observed on various types of porous media (e.g., sandstone, granite, soil and sands) within a temperature range varying between -15 °C and +20 °C (e.g., Coperey et al., 2019; Kemna et al., 2014a; Limbrock and Kemna, 2022; Olhoeft, 1977; Revil et al., 2019; Stillman et al., 2010; Wu et al., 2017). However, SIP signals of natural permafrost soils and rocks during freeze-thaw cycles have rarely been explored. Doetsch et al. (2015) presented IP monitoring data acquired in the Arctic for a period of 4 months during freezing of the ground and hypothesize that changes in Cole-Cole parameters obtained from time-domain IP (TDIP) time-lapse inversions can reliably image freezing patterns. However, in their study, they did not measure the actual frequency dependence of the IP response, but rather assumed a predefined relaxation model to explain the decay curve in TDIP data. To our knowledge, there have been no studies investigating the changes in the frequency dependence of the IP signatures (i.e., SIP signatures) due to subsurface seasonal freezing and thawing processes as well as processes on longer time-scales. Such investigations are important to extend petrophysical models such as the 4PM and PJI to improve ice content estimations taking into account the effect of surface conductivity and its spatial and temporal variability.

In this study, we apply the SIP imaging method in a high mountain permafrost terrain in the Italian Alps, where long-term borehole temperature and meteorological data are available for validation (Pogliotti et al., 2015). In particular, we investigate

the frequency dependence of the imaging results covering a frequency range between 0.1 and 75 Hz for seasonal and annual variations along three years SIP monitoring period. We hypothesize that the frequency dependence of IP resolves temporal changes in the thermal state, and the ice/water ratio of bedrock permafrost and the active layer (changes attributed to seasonal freezing and thawing processes). We propose the use of the phase frequency effect (ϕFE) (the difference in phase between high and low frequencies) as a proxy describing SIP responses without the necessity of fitting a relaxation model (e.g., the Cole-Cole). We demonstrate that such frequency-effect can be used to evaluate seasonal changes in measured and estimated volumetric water content (VWC) and UWC as well as PJI-derived ice content at one time instance. Laboratory results are used to evaluate our field observations, in particular the phase frequency effect.

2 Material and Methods

2.1 Field site

The Cime Bianche monitoring site is located at the Cime Bianche Pass above Cervinia, Aosta Valley (Valtournenche Municipality), in the Italian Alps (Fig. 1) at an altitude of 3100 m a.s.l. (45° 55′09″N, 7° 41′34″E). The lithology of the Cime Bianche plateau is dominated by garnetiferous mica schists, calc-schists and amphibolites with a deeply weathered and fractured bedrock surface. The bedrock surface is covered with a layer of fine-grained to coarse blocky debris deposits with a thickness ranging from a few centimeters to a couple of meters (Pogliotti et al., 2015). Gelifluction lobes, which is a type of mass-wasting, and sorted polygons of fine material indicate the presence of permafrost, which was first recognized in 1990 (Guglielmin and Vannuzzo, 1995). Permafrost monitoring activities started in the late 1990s and the site was consecutively instrumented between 2004 and 2006 by the Environmental Protection Agency of Aosta Valley (ARPA VdA). Temperature measurements are conducted at different depths in a shallow borehole (SBH, reaching a depth of 7 m) and deep borehole (DBH, reaching a depth of 42 m) as well as a spatial grid of ground surface temperature loggers. An automatic weather station continuously monitors air temperature, soil moisture, net radiation, snow depth plus wind speed and direction (Pogliotti et al., 2015; Pellet et al., 2016).

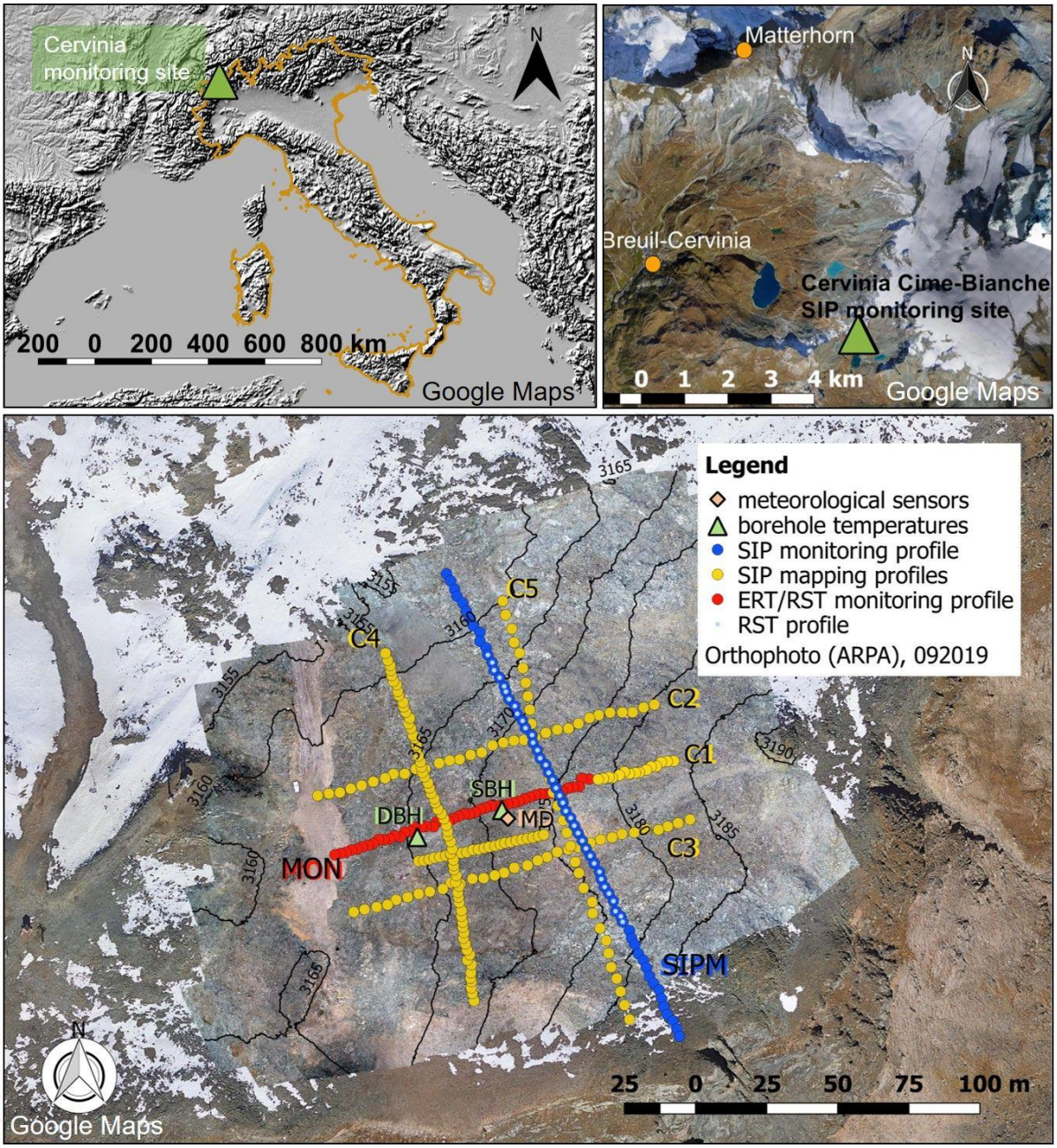

Figure 1: The Cervinia Cime Bianche study site located in the Italian Alps, with the SIP monitoring profile- (SIPM), ERT/RST monitoring profile- (MON), borehole- (shallow borehole (SBH) and deep borehole (DBH)) and meteorological sensors (MD) positions indicated. SIP data were collected along seven profiles: the SIP monitoring profile (SIPM), the SIP profiles C1-C5 collected for a spatial characterization of the site, and the long-term ERT/RST monitoring profile MON (red part of C1). The TINITALY digital elevation model (CC BY 4.0) was used as base layer in panel 1. The satellite background image in panel 3 is overlain by an orthophoto of the survey area including contour lines derived from the digital elevation model (ARPA).

In addition to the thermal and meteorological monitoring, annual ERT and RST (refraction seismic tomography) measurements are collected since 2013 to observe long-term spatio-temporal permafrost dynamics at the site (Pogliotti et al., 2015; Pellet et al., 2016; Mollaret et al., 2019). Mollaret et al. (2019) observed a significant warming in the boreholes and electrical resistivity decrease from August 2013 and 2017 along the entire ERT/RST monitoring profile with estimated maximum ice contents of around 25 % (Mollaret et al., 2020).

2.2 Ground temperatures and meteorological data

During the SIP monitoring period between September 2019 and September 2022, a mean annual air temperature (MAAT) of about -2.3 °C and mean annual precipitation of about 1200 mm yr^{-1} were measured at the site. Strong winds contribute to the spatially changing snow cover thickness at the site with less snow recorded at SBH compared to the DBH (Pogliotti et al., 2015), with a snow cover duration of ~260 days per year within the SIP monitoring period. The borehole temperature data indicate that the permafrost is at least 42 m thick (max. depth of DBH, not shown in Fig. 2) with permafrost temperatures that vary between -0.3 and -1 °C (at 10 m depth, DBH) during the three years. Table 1 summarizes active layer thickness (ALT) evolution for the two boreholes with highest values measured in October 2020 and lowest values reported in October 2021. The observed spatial variability of the ALT between the two boreholes (i.e., ~2.5 m difference in ALT between SBH and DBH in 2021) can most likely be attributed to different ice/water contents due to different surface and subsurface conditions in terms of weathering and fracturing of the bedrock (Pogliotti et al., 2015).

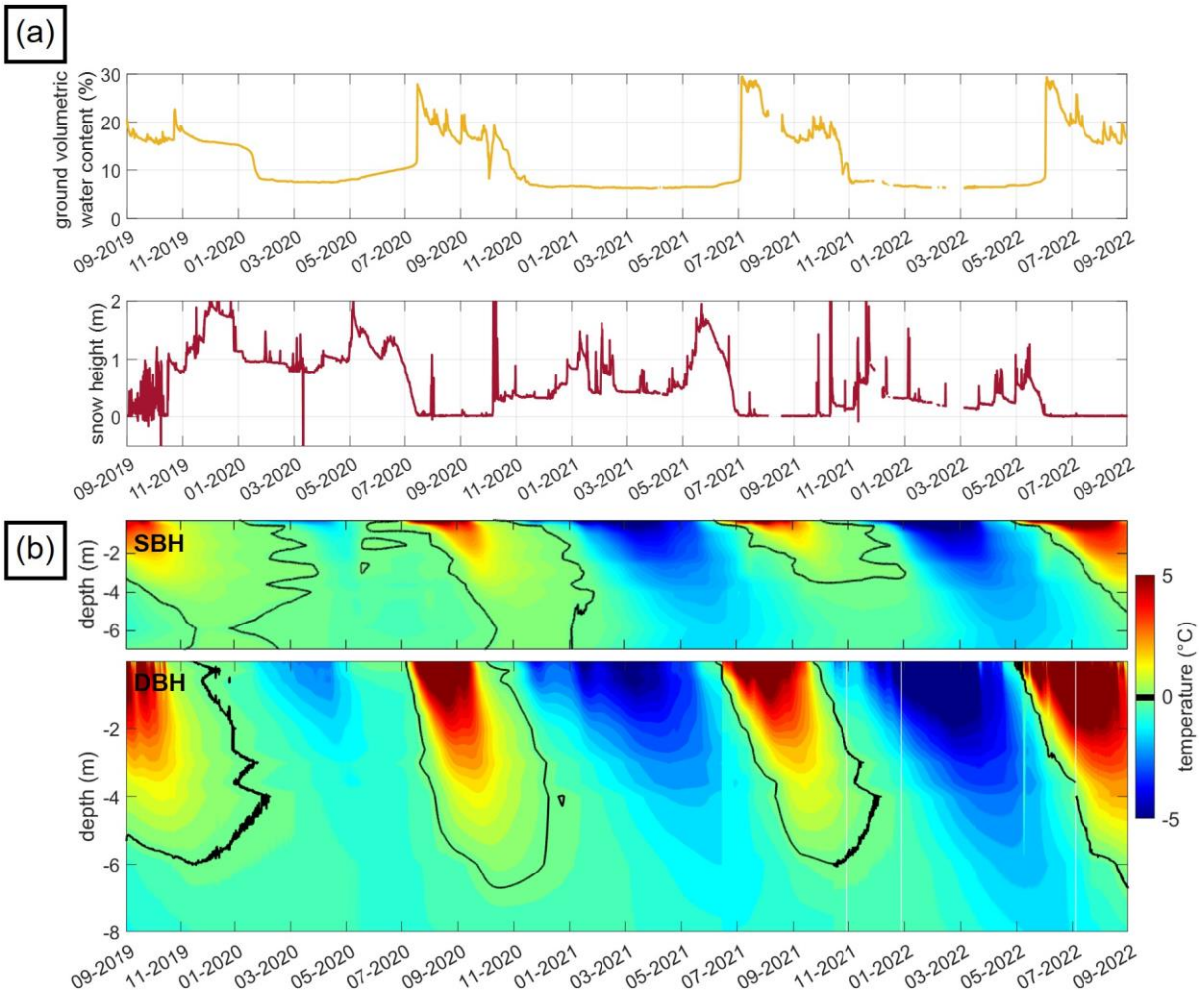

Figure 2: (a) Ground volumetric water content measured at a depth of 20 cm and snow height and (b) borehole temperatures of the DBH and SBH for the SIP monitoring period between October 2019 and November 2022.

Seasonal variations in borehole temperature are consistent and correlate with air temperature, water content and snow height. From Fig. 2, it is seen that the surface was covered by snow for about 260 days a year and with larger average snow heights in winter 2019/20 (0.9 m) compared to 2020/21 (260 days, 0.5 m) and 2021/22 (190 days, 0.2 m). Due to the reduced insulating effect of relatively low snow height (e.g., Zhang, 2005), borehole temperatures reached lowest values in winter 2021/22. The highest air/surface temperatures were recorded in summer 2020 (not shown) And borehole temperatures were highest in summer 2022 (due to earlier snowmelt). During the monitoring period under investigation, the behavior of the VWC is characterized by a steady minimum throughout the winter (6-7.5 %) followed by a strong increase at the beginning of the summer period (~ 20 %) due to snow melt (Fig 2 and Pellet et al., 2016). The highest variability of VWC can be observed during summer when precipitation sums are high.

Table 1: Active layer thickness (ALT) evolution for the SIP monitoring period between October 2019 and August 2022

Year	ALT SBH (m)	ALT SBH (date)	ALT DBH (m)	ALT DBH (date)
2019	-5.9	2019-11-18	-5.9	2019-11-13
2020	-5.9	2020-10-20	-6.7	2020-10-22
2021	-3.5	2021-10-28	-5.9	2021-10-29

2.3 Spectral induced polarization as monitoring method in frozen ground

2.3.1 The complex resistivity method

The induced polarization (IP) method, also referred to as complex resistivity (CR) method is a geophysical electrical technique which is based on measurements of the electrical impedance that can be performed in the time- or frequency domain. When conducted in the frequency domain (as in our study), two electrodes are used to inject a sinusoidal current into the ground and a second pair measures the resultant phase-shifted voltage. The impedance (Z^*) is then given as the amplitude ratio and phase-shift between the measured voltage and the injected current. When performed at different frequencies in the mHz-kHz range, commonly referred to as spectral IP (SIP), information on the frequency dependence of the electrical properties is gained. Multi-electrode measurements, in combination with inversion algorithms (e.g., Binley and Kemna, 2005), permit to resolve for variations of the complex electrical resistivity (ρ^*) (or its inverse, the complex electrical conductivity (σ^*)) in the subsurface (e.g., Kemna et al. 2012). The complex resistivity can be written as its magnitude ($|\rho(\omega)|$) (Ωm) and phase shift (ϕ) (rad) or expressed in terms of the real ($\rho'(\omega)$) (Ωm) and imaginary ($\rho''(\omega)$) (Ωm) components, such as (e.g., Binley and Slater, 2020; Wait, 1984):

$$\frac{1}{\sigma^*(\omega)} = \rho^*(\omega) = \rho'(\omega) + i\rho''(\omega) = |\rho^*(\omega)|e^{i\phi(\omega)}, \quad (1)$$

$$|\rho^*(\omega)| = \sqrt{\rho'(\omega)^2 + \rho''(\omega)^2}\text{, and} \quad (2)$$

$$\phi(\omega) = \arctan\left(\frac{\rho''(\omega)}{\rho'(\omega)}\right), \quad (3)$$

where ω represents the angular frequency ($\omega = 2\pi f$, f the excitation frequency, for low frequencies < 1 kHz) and i is the imaginary unit ($i^2 = -1$). The real and imaginary components of the complex resistivity account for energy loss associated with conduction and energy storage associated with polarization (capacitive property). In natural media, with a negligible amount of electronic conductors, conduction takes place in the pore fluid through the migration of ions (electrolytic conduction, σ_{el}) and within the electrical double layer (EDL) present at the interface between grains and electrolyte (surface conduction, σ'_s) (e.g. Schwarz, 1962; Leroy et al., 2008). The EDL results from the attraction of counterions by charged mineral surfaces, depending on surface charge and surface area. In the presence of an external electric field, charges in the EDL polarize resulting in the polarization effect (measured by the imaginary component of complex conductivity, σ''_s). Accordingly, for frequencies < 1 kHz, the complex conductivity σ^* (or ρ^*)) can be written as (e.g. Binley and Slater, 2020)

$$\sigma^*(\omega) = \left(\sigma_{el} + \sigma'_s(\omega)\right) + \mathrm{i}\sigma''_s(\omega). \quad (4)$$

In the measured frequency band its frequency dependence can often be described by the Cole-Cole model (Cole and Cole, 1941).

Considering that field-SIP devices are often limited in the frequency range and might lack the possibility to recover the frequency maximum required to fit a dispersion model such as the Cole-Cole, we propose here to quantify the frequency dependence in the SIP signatures using the phase frequency-effect (ϕFE). Such parameter represents the difference between the logarithms of the low-frequency and high-frequency ϕ values over a spread of frequencies (A) and normalized by the difference of the logarithms of the two frequencies according to

$$\phi FE = \frac{log_{10}(-\phi(A\omega_0)) - log_{10}(-\phi(\omega_0))}{log_{10}(A\omega_0) - log_{10}(\omega_0)}, \quad (5)$$

where ω_0 is the lowest frequency (in Hz) and the product $A\omega_0$ represents the maximum frequency investigated (in Hz). Grimm and Stillman (2015) proposed a similar analysis but they only took into account the change in electrical resistivity over a spread of frequencies and ignored the polarization parameters (ϕ and σ'').

2.3.2 Temperature dependence of electrical properties

The dependence of rock electrical properties on temperature differs for temperatures above and below the freezing point. Above the freezing temperature, in the presence of liquid pore water in a metal-free porous rock, the bulk electrical conductivity is controlled by the electrolytic conductivity of the liquid pore water and the surface conductivity, while the polarization effect for frequencies below 1 kHz are mainly related to electrochemical (ionic) polarization in the EDL at the pore water - solid matrix interface (Kemna et al., 2012). The temperature dependence of the electrical conductivity is controlled by the temperature dependence of the ionic mobility which is inversely related to the viscosity of the fluid and can be approximated by a linear relationship (Revil and Glover, 1998, 2012; Zisser et al., 2010). Within our analysis we use a model by Oldenborger (2021) for the temperature correction of the bulk electrical resistivity, which can be written as:

$$\rho_{corr} = \rho[1 + \alpha_T(T - T_0) + \beta_T(T - T_0)^2], \quad (6)$$

where α_T and β_T are temperature compensation factors for a fluid that depends on the choice of the reference temperature T_0 and T is the temperature at which ρ is measured. Oldenborger (2021) derived different α_T values of Eq. 6 (i.e., $\alpha_T = 0.02\ °C^{-1},\ T_0 = 20\ °C;\ \alpha_T = 0.0254\ °C^{-1},\ T_0 = 10\ °C; \alpha_T = 0.0321\ °C^{-1},\ T_0 = 0\ °C$).

Binley et al. (2010) measured the change in real and imaginary conductivity with positive temperature and reported an approximate increase of σ' and σ'' (at 1.5 Hz) with temperature of 2 % per °C using Eq. 6. Other empirical formulations modelled the temperature dependence of electrolytic conduction by an Arrhenius-fit (e.g. Oldenborger, 2021).

When water changes its phase from liquid to solid, the salinity of the remaining liquid pore water phase increases (e.g., Hobbs, 1974; McKenzie et al., 2007). Above the eutectic temperature (i.e., the temperature where water starts to crystallize) and below the freezing temperature, ionic exclusion leads to remaining salt within the pore water (e.g., Coperey et al., 2019; Oldenborger and LeBlanc, 2018; Revil et al., 2019) and an increase in fluid conductivity. During ice formation, the decrease in water content

with temperature is gradual and follows a freezing curve (or thawing curve), where no super-cooling is present (e.g., McKenzie et al., 2007). The saline unfrozen water is composed of residual water films (i.e., bound water) at the ice and mineral surfaces and water in smaller pores with a reduced melting point related to capillary and adsorptive forces according to the Gibbs-Thomson effect (see, e.g., Dash et al., 2006; Kemna et al., 2014a; Mohammed et al., 2018). Duvillard et al. (2018) and Coperey et al. (2019) extended the Stern-layer model of Revil (2012, 2013b, 2013a) to freezing conditions to describe the dependence of the electrical conductivity and the normalized chargeability on temperature below 0 °C including parameters as the residual water content, porosity, freezing and characteristic temperature. Similar resistivity-temperature models were used to account for the temperature dependence of the electrical resistivity upon freezing for geophysical investigations in permafrost terrain (Oldenborger and LeBlanc 2018; Oldenborger, 2021).

2.3.3 Prediction of unfrozen water content and volumetric water content from petrophysical relationships

The distribution of subsurface electrical resistivity depends on soil properties such as saturation (S_w), fluid resistivity (ρ_w) or conductivity (σ_w) porosity (Φ) and surface conduction (σ_s') (e.g., Lesmes and Frye, 2001), which can be written as:

$$\sigma_b = S_w^n \Phi^m \sigma_w + \sigma_s' \quad (7)$$

where m is defined as the cementation exponent and n is the saturation exponent. While the saturation exponent varies in the range $n = 2 \pm \frac{1}{2}$, the cementation exponent can range from 1 (for rocks with a low porosity but well-developed fracture network) to around 5 (for rocks with a low connectedness of the pore and fracture network) (Glover, 2009).

Neglecting surface conduction, Oldenborger (2021) computes the volumetric water content (in percent) as a function of porosity and saturation (S_w), such as:

$$VWC = (S_w \cdot \Phi) \cdot 100, \quad (8)$$

with saturation being resolved from ERT data using the following relationship:

$$s_w = \sqrt[n]{\frac{\rho_w}{\Phi^m \cdot \rho_{corr}}}. \quad (9)$$

Within our study, we used the same value (i.e., 100 Ωm) for the pore water resistivity (ρ_w) as previous studies at the site (Mollaret et al., 2020) and estimated the cementation exponent for a given measurement of VWC, with a constant factor $a = 1$ and assuming $n = 2$. In Eq. 9, ρ_{corr} is the temperature-corrected bulk electrical resistivity at 0.5 Hz of Eq. 6. Upon freezing, S_w decreases and ρ_w increases due to ionic exclusion and estimates of the unfrozen water content S_0, which is the fraction of water remaining unfrozen even at relatively low temperatures, can be derived by (Daniels et al., 1976)

$$S_0^{(1-n)} = \frac{\rho_F}{\rho_0} \quad , \quad (10)$$

with ρ_F being the resistivity of frozen and ρ_0 of unfrozen material for which it is assumed that the pore space was completely saturated prior to freezing ($S_0 = 1$). Using an exponential relationship for subfreezing temperatures,

$$\rho = \rho_0 e^{b(T_F - T)}, \quad (11)$$

Hauck (2002) and Oldenborger and LeBlanc (2018) derived estimates of the unfrozen water content as follows

$$S_0 = e^{\frac{b(T_F - T)}{1-n}} \quad , \tag{12}$$

with the constant b being a function of depth.

2.3.4 Monitoring set-up and acquisition of SIP imaging data

An array of 64 stainless steel electrodes with a separation of 3 m between electrodes connected with coaxial (shielded) cables, resulting in a profile length of 189 m was permanently installed in October 2019 at the Cime Bianche plateau. The position of the SIP monitoring (SIPM) profile was chosen away from boreholes (c.f. Figure 1) and other metallic structures to avoid interferences due to electronic conduction. The position of the profile aimed at covering different surface characteristics, namely fine-grained, coarse-blocky areas and parts dominated by bedrock outcrops found along the study area towards the understanding of spatio-temporal SIP imaging results associated to different substrates during the SIP monitoring period.

Measurements were conducted with an eight-channel data acquisition system (DAS-1 manufactured by Multi-Phase Technologies). The configuration protocols consisted of dipole-dipole (DD) and multiple gradient (MG) arrays and deployed coaxial cables to reduce cross-talking (e.g., Flores Orozco et al., 2013). During the SIP monitoring period, between October 2019 and August 2022, SIP data were collected at 12 different frequencies in the range between 0.1-225 Hz using a DD configuration with dipole lengths of 12 m (skip-3) as normal and reciprocal (N&R) pairs for the quantification of data error (e.g., LaBrecque et al., 1996; Flores Orozco et al., 2012; Slater et al., 2000) yielding a total number of 1474 quadrupoles (Table A, Appendix). The MG configuration was deployed with a total number of 744 quadrupoles using 4 potential dipole lengths of 3 m, 6 m, 9 m and 12 m within the current dipole in order to collect data sets with a higher signal-to-noise ratio (e.g., Dahlin & Zhou 2006) compared to the DD configuration. These MG setup performed better during the winter period (between November and June), as poor galvanic contact between electrodes and the ground (also called contact resistance R_s) and low current densities injected in frozen terrain covered by snow, deteriorated the quality of the DD measurements. Mean current injections (I) varied between 0.2-15 mA throughout the whole SIP monitoring period and are listed for every measurement date in Table A in the Appendix.

R_s were recorded before each data acquisition with observed mean values between 20-160 kΩ and. The highest R_s values were measured in the coarse-blocky part with observed values of 30-90 kΩ in the summer period and 125-190 kΩ in the winter months. Lowest values were observed for electrodes located in the fine-grained part of the profile with R_s values between 5-20 kΩ in summer and between 40-90 kΩ in winter.

During the SIP monitoring period, we avoided artificially wetting the electrodes for a reduction of R_s (e.g., Mollaret et al., 2019; Maierhofer et al., 2022), to ensure comparable conditions throughout the year (as proposed by e.g. Hilbich et al., 2011). We aimed at collecting an entire SIP data set once a month during a period of 2 years (between October 2019 and October 2021), to capture seasonal and annual changes in the polarization response. However, inaccessibility to the study area during the COVID-19 Pandemic and technical problems lead to gaps in the SIP monitoring data in December 2019 and December

2020, as well as to the period between March and June 2020. In addition to the monthly measurements, we collected another end-of-summer dataset in August 2022.

2.3.5 Data filtering, data error analysis and inversion procedure of SIP monitoring data

We processed DD and MG data for every frequency and monitoring date independently, following the automated processing procedure presented in Fig. 3. For all DD data sets, we removed as erroneous readings those values related to $R_s > 200$ kΩ (are considered as open circuit) and/or negative impedance magnitude (Z) values, as well as positive impedance phase values (ϕ). In case of DD measurements, outliers were identified (and removed) as those quadrupoles for which the misfit between normal and reciprocal impedance magnitude (ΔZ) and phase ($\Delta\phi$) readings was larger than 50% of the average value (Z_{NR}, ϕ_{NR}) and larger than twice the standard deviation of the N&R misfit of the entire data set, similar to Maierhofer et al. (2022). For MG surveys, where no reciprocals were measured, we developed an analysis scheme for data quality that considers the relationship between phase and voltage readings to assess signal strength and a moving average filter to remove spatial outliers and erroneous measurements (c.f., Fig 3). In other words, we removed isolated readings based on plots from phase readings plotted against their associated voltages. The resulting numbers of data after filtering are summarised in Table A (Appendix) for each survey.

After the analysis of the independent data sets, we analysed the temporal evolution of the number of quadrupoles for each frequency. This is needed to warranty that imaging results obtained from different times are related to similar resolution. Due to the high number of outliers detected for winter measurements (up to 80% for 75 Hz), we did not systematically remove unrepeated quadrupoles for the entire SIP monitoring period. We performed analysis for detailed processes: (1) the thawing of the active layer during the summer period (June to October 2020), and (2) the inter-annual changes based on summer measurements (August 2020, 2021 and 2022). For those two specific analyses, only repeated quadrupoles were used for inversion.

The N&R analysis revealed a significant increase of 30-50 % in the error parameters for the winter measurements demonstrating lower S/N in winter and higher uncertainties in the imaging results obtained for measurements between January and May. Different SIP monitoring studies (e.g., Lesparre et al. 2017, Flores Orozco et al., 2019) use the same error parameters for the inversion of the entire monitoring period assuming that this permits the comparison of imaging results obtained with the same level of contrasts, i.e., sensitivity. However, such an approach assumes fairly consistent S/N across the monitoring data set. Accordingly, within our analysis, assuming the same error parameters for the entire SIP monitoring period lead to either under-fitting the readings in summer (assuming the error level from winter measurements), or over-fitting the winter data when inverted to the error parameters observed in summer measurements. Hence, we define error parameters for each data set collected at different times and frequencies, which also considers the frequency dependence observed in our data with higher misfits detected for higher frequencies compared to lower frequencies (similar to Flores Orozco et al., 2011). Additionally, we used the same error parameters for DD and MG data, since error models allow the use of the same error parameters for configurations where no reciprocals are available.

For the inversion of the SIP data, we used the finite-element smoothness-constraint inversion code CRTomo (Kemna, 2000), which computes the distribution of the complex resistivity in the subsurface from a given data set of impedance magnitude and phase values at a distinct frequency. Data-error estimates are defined in the inversion and permit to fit the observed data within its noise level, which is defined by the error model (Kemna, 2000). The iteration is stopped if the RMS difference between model response and data which includes a normalization of the individual misfits by the error taken from the error model reaches a value below its target value of 1, after which smoothing is again increased until the RMS value is equal to 1 (within a tolerance interval). The inversions converge to the target value fitting the observed data within their estimated noise level for the smoothest possible model.

To assess the reliability of the monitoring inversion results, especially regarding the resolved electrical properties at depth, we make use of the depth of investigation (DOI) index, introduced by Oldenburg and Li (1999). In our analysis, we calculated the DOI index for resistivity and phase images $m_1(x,z)$ and $m_2(x,z)$ for all frequencies as

$$DOI(x,z) = \frac{m_1(x,z) - m_2(x,z)}{m_{1r} - m_{2r}} \quad (14)$$

with constant reference models of $m_{1\mathrm{r}} = 1000\ \Omega\mathrm{m}, -5\ \mathrm{mrad}$ and $m_{2\mathrm{r}} = 10\,000\ \Omega\mathrm{m}, -75\ \mathrm{mrad}$. DOI values are computed for resistivity and phase images and applied separately to the corresponding images. We chose the values of the reference models as mean minimum and maximum resistivity and phase values observed in all SIP images. We blank model regions with large DOI values (i.e., > 0.2 as proposed by Oldenburg and Li, 1999) in all imaging results presented in this study.

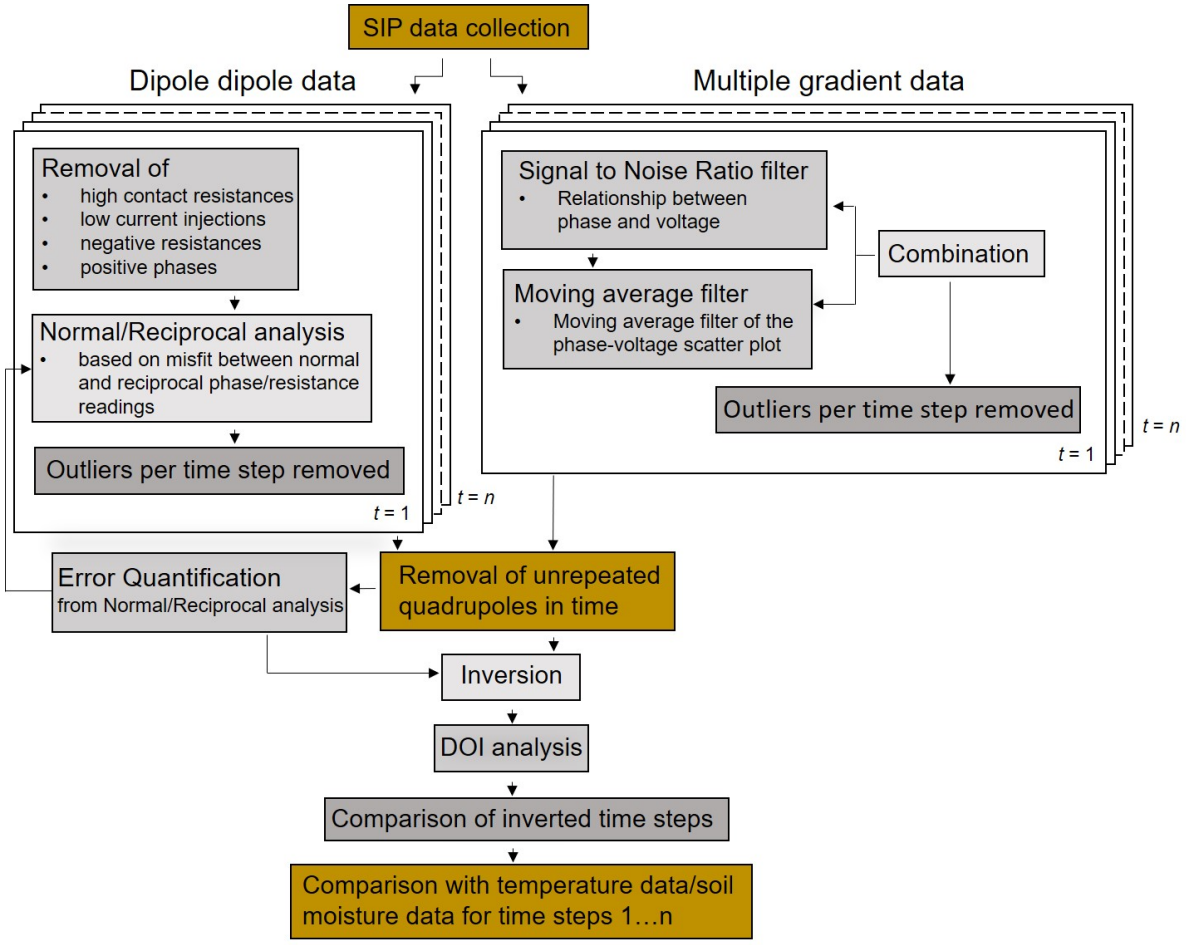

Figure 3: Work flow of SIP data processing for the monitoring data set at Cime Bianche, Cervinia.

2.4 Complementary geophysical datasets

In September 2019, we collected ERT data along five profiles C1, C2, C3, C4 and C5 (Fig. 1), using the DAS-1 device with a DD configuration with dipole lengths of 12 m (skip-3). For profiles C2, C3 and C5, 32 electrodes and a separation of 4 m was chosen, whereas profiles C1 (prolongation of the ERT/RST monitoring profile) and C4 consist of 64 electrodes and 2 m separation. Data quality was evaluated by means of N&R analysis and the inversion of the resistivity data at 0.5 Hz was performed in 3D using the modules of the open-source library pyGIMLi (Rücker et al., 2017). We used mean error parameters (a=0.1 Ω, b=5 %) from N&R analysis for the inversion of the ERT data sets to fit all data to the same error level enabling a better comparison of the multi-dimensional (different profiles and frequencies) inversion results similar to Lesparre et al. (2017).

Refraction seismic tomography (RST) measurements were conducted along the SIP monitoring profile in August 2020 with a 24-channel Geode instrument (manufactured by Geometrics) and 24 geophones (corner frequency of 30 Hz) with a roll-along of 12-geophones overlap. In total, 36 receiver and 14 shot locations were used with ~15 individual shots recorded between electrode 12 and 48 (between profile meter 33 to 141) keeping the same geophone spacing as for electrodes. We used a sledgehammer as source of the seismic waves with hit points between every second geophone along the seismic refraction line. The individual shots were stacked ~10 times to improve the signal-to-noise ratio of the seismic data. First-break travel time picking was manually done using the open-source library formikoj (Steiner and Flores Orozco, 2023) which provides modelling, reading and basic processing of seismic waveform data. A 120 Hz low-pass filter was applied to the seismic traces to mitigate the influence of high-frequency noise. For the independent inversion of the picked P-wave travel times we used the modules of the open-source library pyGIMLi with an estimated RST data error of 2.2 ms from comparing a subset of travel times that was picked twice.

We used the PJI framework developed by Wagner et al. (2019) to quantify the four volumetric fractions of ice (f_i), water (f_w), air (f_a) and rock matrix (f_r), based on the filtered apparent resistivity values and picked P-wave travel times. We used the same porosity and seismic velocity values as in Mollaret et al. (2020), i.e. an initial porosity of 40 % and constituent velocities (v_p) of 1500 m/s for pore water, 3750 m/s for ice, 4000 m/s for the rock matrix and 330 m/s for air. We accounted for surface conductivity in addition to electrolytic conduction by introducing a constant surface conductivity term in Archie's law. We used a surface conductivity range between 0.001 and 0.01 S/m (based on laboratory studies on pure ice (Bullemer and Riehl 1966; Carantl and Illlngworth 1982) and rock samples under freezing conditions (Coperey et al., 2019)) and chose a final constant value across the imaging plane of 0.01 S/m as it resulted in the lowest chi-square (χ^2). A relative error of 5 % was used for the ERT data following the N&R analysis and an absolute error of 2.2 ms for the picked travel times in the inversion, which resulted in an error-weighted χ^2 fit of 1.0. The final PJI results are presented in Appendix C.

2.5 Complementary SIP laboratory data

Laboratory measurements were performed on a cylindrical solid rock sample of 10 cm length and 3 cm diameter of amphibolite (with a porosity of 3.5 %) and a loose sediment surface sample, both collected close to the SIP monitoring profile. The electrical impedance was measured in a frequency range of 10 mHz to 45 kHz during controlled freeze-thaw cycles (+20°C to -40°C to +20°C), using a 4-channel SIP-04 impedance spectrometer (Zimmermann et al., 2008) and is shown in the Appendix B. The solid rock sample was fully saturated with water of similar fluid conductivity as in field conditions (0.01 S/m). For this purpose, diluted tap water was used to obtain an electrolyte with a distribution of ions that resembles realistic field conditions. Afterwards, the sample was sealed in a shrinking tube, and placed in a climate chamber where it was cooled down from +20°C to -40°C by successively changing the temperature in steps of 0.2°C - 4°C with a duration of 120 to 180 minutes for each temperature step. Limbrock and Kemna (2022) found such settings to be sufficient for the given size and thermal properties of the sample to reach thermal equilibrium. After one freezing cycle, the samples were heated up again following the same

temperature procedure. For potential measurements, we used ring electrodes made out of tinned copper with a distance of 3 cm. The loose sediment sample was saturated up to a volumetric water content of about 20%, with the same type of water and placed in a cylindrical container with a total length of 18 cm, a diameter of 4 cm, and a potential electrode separation of 6 cm. Due to the increased sample size, the duration of each temperature step was increased by 60 minutes.

3 Results

3.1 Site characterization

In Fig. 4, we present 3D electrical resistivity results as slices extracted at different depths parallel to the surface obtained from the 3D inversion of the five ERT profiles (C1-C5) collected in September 2019. Fig. 4 shows lower electrical resistivity values in the shallow subsurface (0 - 4 m depth) than for deeper layers (> 5 m depth), with slightly lower values observed in the western compared to the eastern part of the study area. The thickness of the low-resistive surface layer (inflection point in electrical resistivity) is slightly overestimated compared to the thaw depth measured in the boreholes at the date of the geophysical measurements (Fig. 4g) most likely due to the smoothing in the inversion. Low electrical resistivity values (< 8000 Ωm) are observed in the northern and the central-western part of the study area for all depths; whereas the highest electrical resistivity values (~ 30000 Ωm) are observed at > 5 m depth in the central, central-eastern and central-southern parts of the study area. Between 6 and 20 m depth we observe no strong resistivity changes associated to the permafrost body.

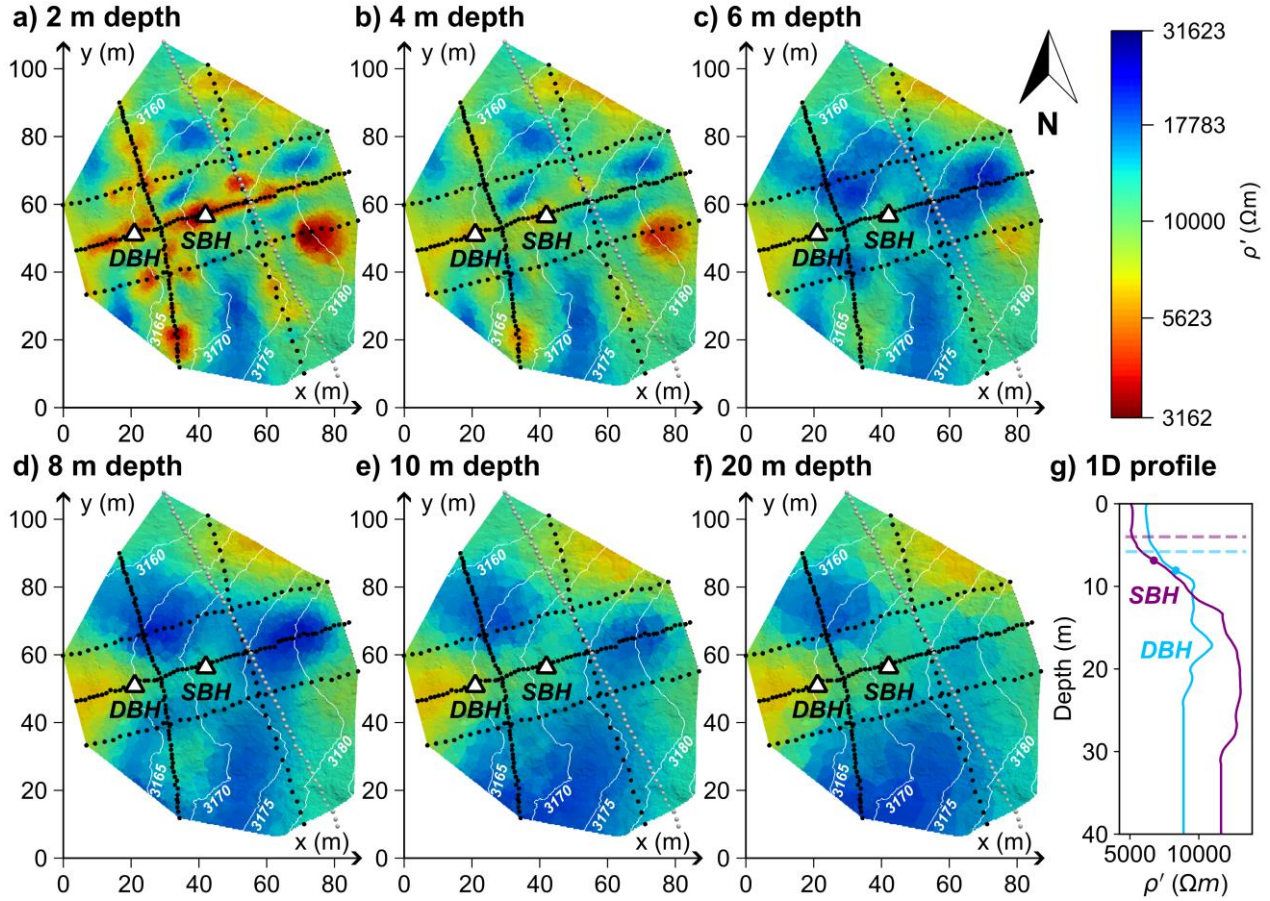

Figure 4: Spatial characterization of the Cime Bianche monitoring site based on the 3D electrical resistivity inversion results from five profiles collected in September 2020 (dotted black lines). Panels a)-f) represent slices parallel to the surface in six different depths. The borehole location of the SBH and the DBH are marked and white contour lines represent the surface elevation. The coordinates of the SIP monitoring profile are shown in addition (dotted grey line), but these data were not used for inversion due to a differing measurement date (October 2020). Panel g) represents the resistivity-depth profiles at the location of the two boreholes with the measured thaw depth (dashed lines) and the inflection point in the resistivity data (dots).

The baseline SIP imaging results along the permanent SIP monitoring profile of October 2019 are presented in Fig. 5 expressed in terms of the phase (ϕ), the real (ρ') and imaginary (ρ'') components of the CR, obtained for data collected along the SIP monitoring profile for low (0.5 Hz) and high (75 Hz) frequencies. While the frequency dependence is pronounced in the polarization parameters (for ρ'' and ϕ), we observe no variation in ρ' with increasing frequency for the whole imaging plane. Similar to the results shown in Maierhofer et al. (2022), absolute ρ'' and ϕ values are higher for 75 Hz (hereafter ${\rho_{75}}''$ and ϕ_{75}) than for 0.5 Hz (${\rho_{0.5}}''$ and $\phi_{0.5}$). Comparatively low values are resolved at depths < 4 m for ${\rho_{0.5}}'$, ${\rho_{75}}''$, and ϕ_{75} and < 5 m for $\phi_{0.5}$, which can be related to the 4 m thick thaw layer composed of fine- to coarse-grained material (see the surface characteristics shown in Fig. 5a). The thaw layer is underlain by a high-resistivity layer with high absolute $\phi_{0.5}$ and ϕ_{75} values, which is representative for the permafrost body (e.g. Table 2). The contrast between the two layers is highest for ${\rho_{0.5}}'$ and ϕ_{75}.

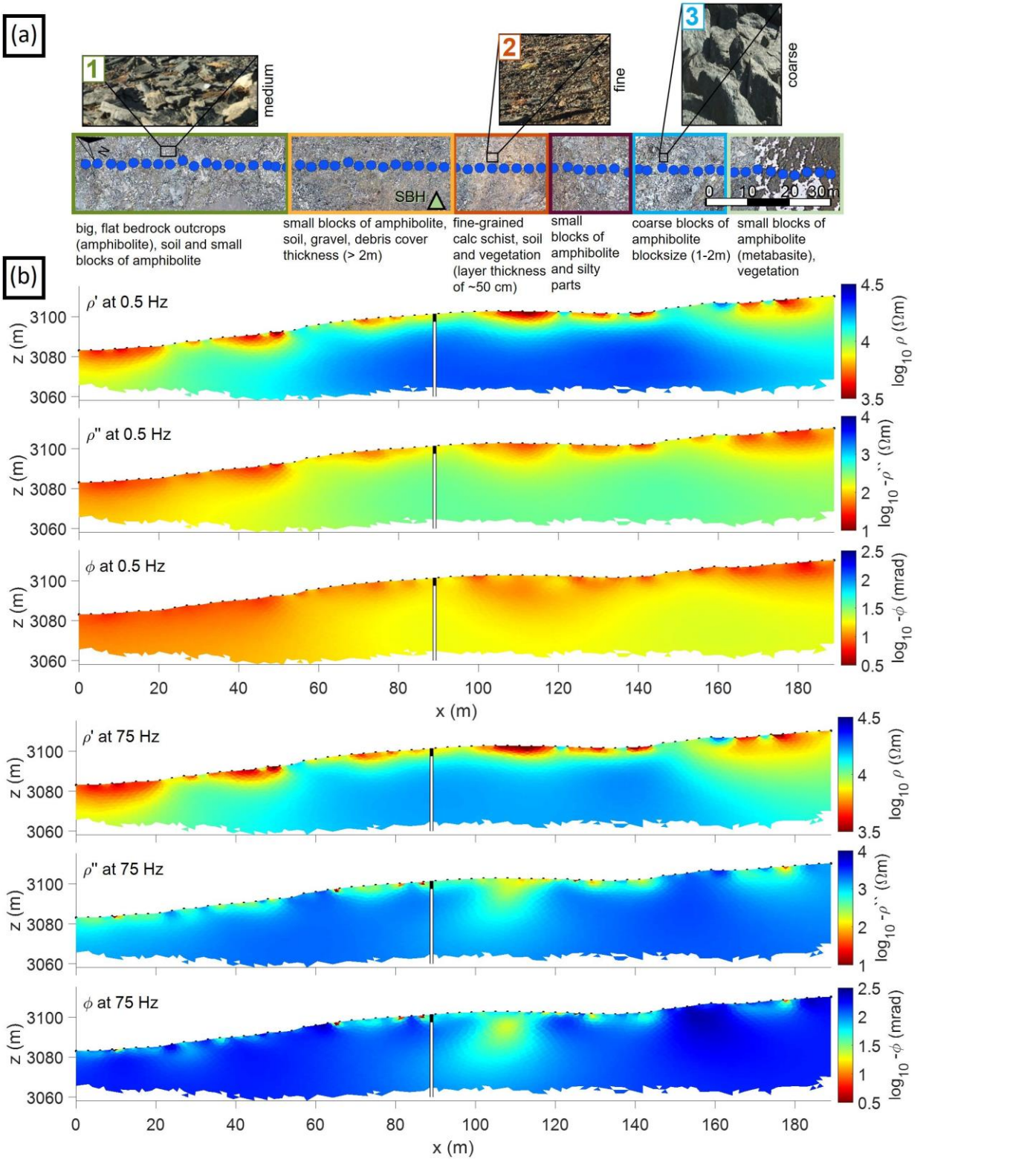
(a)
1
medium
2
fine
3
coarse
SBH
0 10 20 30 m
big, flat bedrock outcrops (amphibolite), soil and small blocks of amphibolite
small blocks of amphibolite, soil, gravel, debris cover thickness (> 2m)
fine-grained calc schist, soil and vegetation (layer thickness of ~50 cm)
small blocks of amphibolite and silty parts
coarse blocks of amphibolite blocksize (1-2m)
small blocks of amphibolite (metabasite), vegetation
(b)
ρ' at 0.5 Hz
ρ'' at 0.5 Hz
ϕ at 0.5 Hz
ρ' at 75 Hz
ρ'' at 75 Hz
ϕ at 75 Hz
z (m)
x (m)
log10 ρ (Ωm)
log10 -ρ'' (Ωm)
log10 -ϕ (mrad)

405

Figure 5: SIP baseline imaging results, corresponding to data collected in October 2019. Panel a) represents different substrate classes, which are discussed in more detail in the Discussion Section. (b) Baseline complex resistivity model (October 2019) at two frequencies (0.5 Hz and 75 Hz) with the two boreholes located at the center of the profile (the SBH 20 m away, the DBH 50 m away), and the black layer representing the thaw depth at the measurement date.

Concerning lateral changes in the SIP images, the highest electrical resistivity and absolute phase values are observed for all depths between profile meter 138 and 162 (e.g. PF 3 in Table 2) corresponding to the coarsest amphibolite blocks of 1-2 m size found at the surface of the SIP monitoring profile (see Fig. 5a). The uppermost 1-3 m of profile meter 93 to 117 reveal the lowest resistivity values and absolute phase values at 75 Hz (e.g. PF 2 in Table 2) along the profile, which can be related to a thin layer of silty soil with some vegetation and fine-grained calc-schists observed at the surface (see Fig. 5a). The contrast to the frozen bedrock is clearly visible for this part of the profile for all components of the complex resistivity except for ρ_{75}'' and ϕ_{75}, where we resolve a low-polarizable anomaly also at depth ($\rho_{75}'' < 1100$ Ωm, $\phi_{75} < 60$ mrad). In the northern part of the monitoring profile with intermediate grain size (between 0 and 51 m), we observe low real resistivities and absolute phase values at the surface (e.g. AL 1 in Table 2) and at depth (e.g. PF 1 in Table 2) for 0.5 Hz and intermediate absolute phase values for 75 Hz (see Table 2).

Table 2: Range of complex resistivity values observed along the SIP monitoring profile for different substrate classes

Subsurface materials	$\rho_{0.5}'$ (Ωm)	$\rho_{0.5}''$ (Ωm)	ρ_{75}'' (Ωm)	$\phi_{0.5}$(mrad)	ϕ_{75} (mrad)
AL 1	$5000-10000$	$40-70$	$300-800$	~5	$40-70$
AL 2	$3000-6500$	$60-80$	$100-500$	$5-10$	$30-60$
AL 3	$8000-12500$	$70-120$	$1100-1600$	$5-15$	$120-200$
PF 1	$6500-15000$	$70-140$	$500-1600$	$5-10$	$100-160$
PF 2	$3000-20000$	$80-160$	$400-1100$	$5-15$	$40-100$
PF 3	$10000-20000$	$100-300$	~1500	$10-15$	$120-250$

3.2 The temperature dependence of the SIP method

Fig. 5 reveals clear variations in the polarization for different depths (i.e., temperatures) and frequencies. To better understand the temperature dependence of the polarization response, we show in Fig. 6a the measured impedance field data (apparent resistivity magnitude ρ_{app} and phase ϕ_{app}) in the active layer in a frequency range of 1-75 Hz between October 2019 and November 2021 including warm (i.e., summer months July to October) and cold (i.e., winter months November to May) periods. For comparison, Fig. 6b shows SIP laboratory data in the same frequency range measured over a thawing cycle from -10 °C to +10 °C.

For both laboratory and field data, we observe a clear distinction in the polarization response between unfrozen and frozen states. Absolute phase values are low for positive temperatures (summer months) and show no significant frequency -dependence; whereas if temperature decreases (during winter) we observe an increase in absolute ϕ_{app} values eight times

higher than in unfrozen state between 1 and 75 Hz. This increase in absolute phase for subfreezing temperatures starts at a frequency of 7.5 Hz for the field data, at ~10 Hz for the loose sediment sample and at ~50 Hz for the solid rock sample. Thus, the inflection point seems to change depending on the texture/ice content. Such effect can be related to the well-known temperature-dependent relaxation behaviour of ice with its maximum in the kHz range (as shown for the full spectrum between 10 mHz and 45 kHz in Appendix B). Additionally, the increase in absolute ϕ_{app} values with increasing frequency is more pronounced for the loose sediment sample (45 mrad at -10 °C) than for the solid rock sample (15 mrad at -10 °C), suggesting an enhanced response with increasing ice contents. Accordingly, the frequency dependence in the phase measurements might be used as proxy to discriminate between regions with no ice and regions richer in ice, as also observed in Maierhofer et al. (2022). Clearly, the frequency range in the SIP data needs to extend above this sensitive frequency, which corresponds to an inflection point between the low response (likely due to the geology) and the high values associated to ice. When comparing the SIP monitoring and laboratory data, we find a similar behaviour in the polarization during freezing and thawing cycles, however, the increase in absolute phase is smaller for laboratory data (2-15/5-45 mrad for the rock/sediment sample) than for field data (35-290 mrad) in the temperature range covered by both data sets (-8 to +10°C observed within the active layer at our field site).

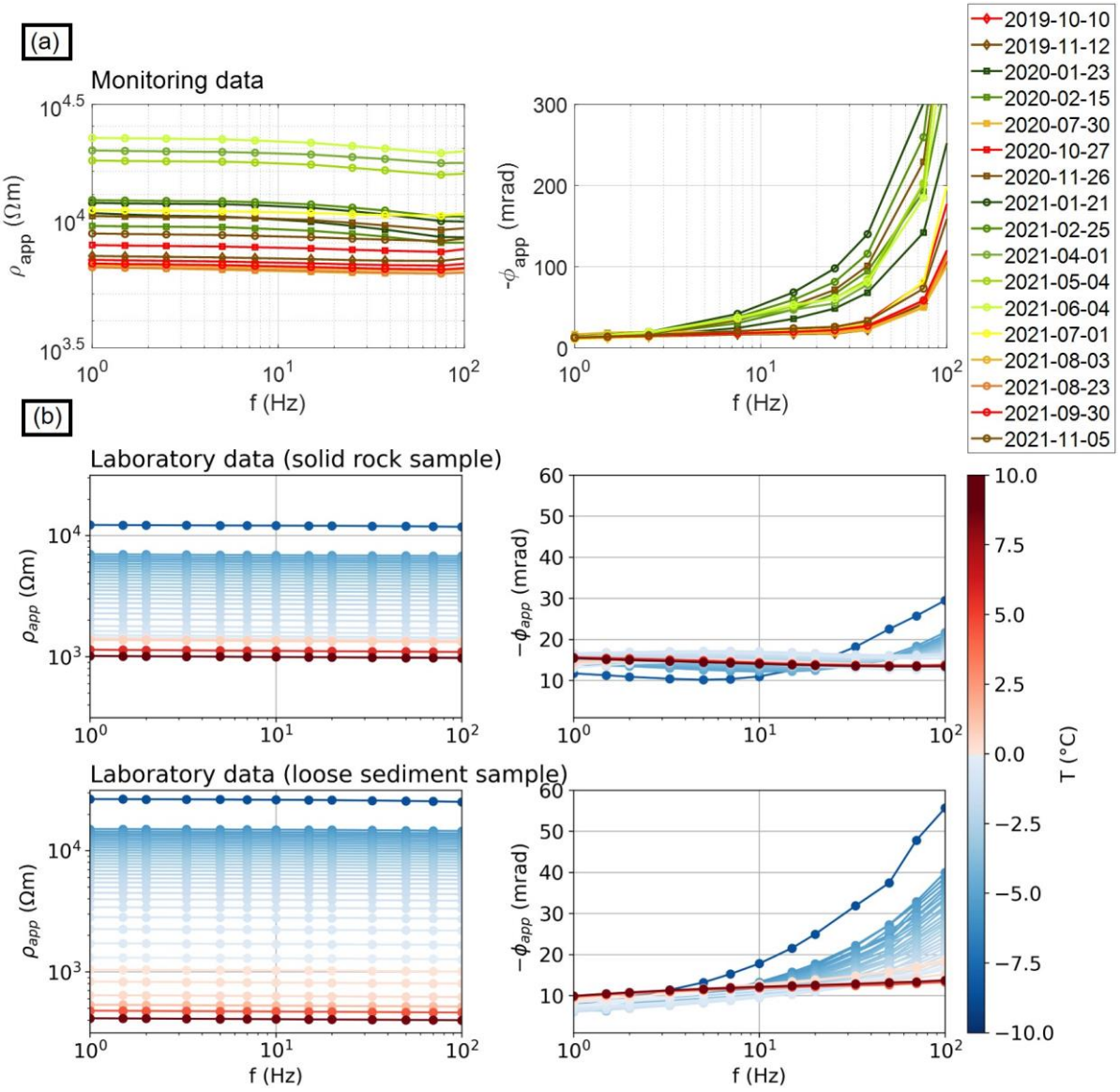

Figure 6: (a) Temporal changes of SIP measurements between October 2019 and November 2021 (frequency range: 0.5-75 Hz). Impedance magnitude expressed in terms of its phase and magnitude (converted to apparent resistivity) values and shown for level 1 and 2 (i.e. 3 and 6 m electrode separation between current and potential dipoles, which corresponds to the active layer) at a horizontal distance of 80 m. Different symbols and colors representing different years and months, respectively. Variations in ρ_{app} and ϕ_{app} between summer and winter are linked to seasonal temperature variations between +10 and -8 °C measured in the borehole close to the subsurface. (b) SIP laboratory measurements on a solid rock sample and a loose sediment sample collected at the site close to the monitoring profile for a frequency range between 1 Hz and 75 Hz and temperatures between -10 °C and +10 °C.

3.3 The phase frequency effect and its link to temperature, water content and ice content estimates

Figure 6a shows that our SIP field data do not capture the peak in the frequency dependence, which according to e.g. Auty and Cole (1952) would be expected between 4 and 11 kHz for pure ice, but extend above the inflection point associated to a

sensitive frequency, where phase values increase with increasing frequency and ice content. Hence, we propose to analyze the phase frequency effect (ϕFE) presented in Equation 5. To evaluate the applicability of such parameter, we present in Fig. 7 the lab measurements collected during (7a) freezing and (7b) thawing cycles in terms of apparent resistivity (ρ_{app} at 0.5 Hz) and for the ϕFE (calculated between 70 and 0.5 Hz).

After saturating and cooling both samples from +10 °C to ~0 °C, both ρ_{app} and ϕFE follow a linear trend, with values increasing with decreasing temperature. During initial freezing, supercooled conditions with constant ρ_{app} and ϕFE values occur between 0 °C and -2.8 °C for the loose sediment sample, and between 0 °C and -2.8 °C for the solid rock sample. An exponential increase in ρ_{app} (3 $k\Omega m/°C$ for the sediment sample, 1.9 $k\Omega m/°C$ for the rock sample) and ϕFE (0.044 per °C for the sediment sample, 0.031 per °C for the rock sample) is observed below this temperature, which is indicative of abrupt ice formation in the pores of the samples. During thawing from -10°C to -0.1 °C (for the loose sediment sample) respectively -0.7 °C (for the solid rock sample), ρ_{app} and ϕFE gradually decrease with a smaller average rate of change for the rock sample (1.4 $k\Omega m/°C, 0.021\ per\ °C$) than for the sediment sample (3 $k\Omega m/°C, 0.03\ per\ °C$), suggesting continuous melting of ice in the pore space.

During thawing, ρ_{app} and ϕFE are generally higher than during freezing ($\Delta\phi FE = 0.05$). Upon freezing, supercooling leads to a remaining unfrozen pore fluid below the freezing point until ice starts to form, thus, resulting in a larger amount of unfrozen water compared to thawing processes at the same temperature (Wu et al., 2017). Additionally, we observe a lowering of the freezing point of water due to ions being excluded from ice formation and accumulating in the liquid phase (Bittelli et al., 2004). At subfreezing temperatures, ρ_{app} and ϕFE values are generally higher for the loose sediment sample, which can be explained by a higher ice content of the loose sediment sample compared to the solid rock sample. Hence, from Fig. 7 we depict a clear dependence of the ϕFE on temperature and ice content.

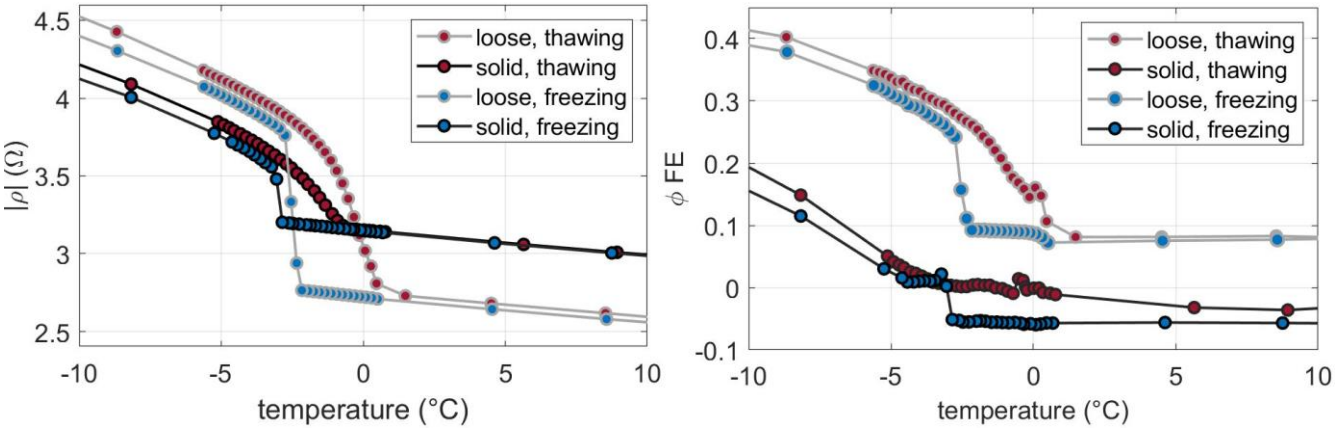

Figure 7: Temperature dependence of a) the impedance magnitude (at 0.5 Hz) and b) for the ϕFE (calculated between 70 and 0.5 Hz) measured on solid rock (solid) and loose sediment (loose) samples during freezing (blue) and thawing (red) in the laboratory (same experiments as shown in Fig. 6).

Fig. 8 shows the spatial variation in the ϕFE computed from the inversion of field data collected in August 2020 along the SIP monitoring profile. To investigate a possible correlation with ice and water content, we compare this image with PJI-estimated volumetric ice and water contents (f_i, f_w) based on ERT and RST data collected on the same day in the same profile. The complete PJI results (electrical resistivity, seismic velocities as well as rock and air contents) are presented in Appendix B. The ϕFE in Fig. 8c ranges from 0.2 to 0.4, similar to the values observed in the laboratory, and is highest at 5-10 m depth (~ 0.35 at the borehole location) and lowest in the thaw layer (< 0.3 at the borehole location). Fig. 8a-b reveal that PJI-estimated f_i values are minimal (~7-10 %) and f_w reaches its maximum (10-33 %) in the thaw layer. Highest f_i (~ 22 % at the borehole location) and lowest f_w (~ 4 % at the borehole location) are encountered between 5 to 10 m depth. The comparison of vertical 1D logs of ϕFE, f_i (Fig. 8d) and f_w (Fig. 8e) at the borehole location suggests a high and positive linear correlation between ϕFE and f_i ($r^2 = 0.9$), and a lower and negative correlation between ϕFE and f_w ($r^2 = 0.5$). In general, there is a good correlation between low ϕFE and low f_i, and high f_w; while high ϕFE correspond also with high f_i, and low f_w, supporting our hypothesis that the phase frequency effect can be used as a proxy for the ice content – and indirectly temperature and water content. The main inconsistency between the three parameters can be observed between 90 and 115 m, where a low-ϕFE anomaly coincides with high f_i. Within this part of the profile, we observe at the surface the material with the finest texture (i.e., silty soil, box 2 in subpanel (5a)) with calc schists visible at the surface. Hence, the polarization parameter might be able to resolve a decrease in ice content that the PJI is not able to resolve due to the lack of sensitivity of electrical resistivity and seismic velocities to textural properties.

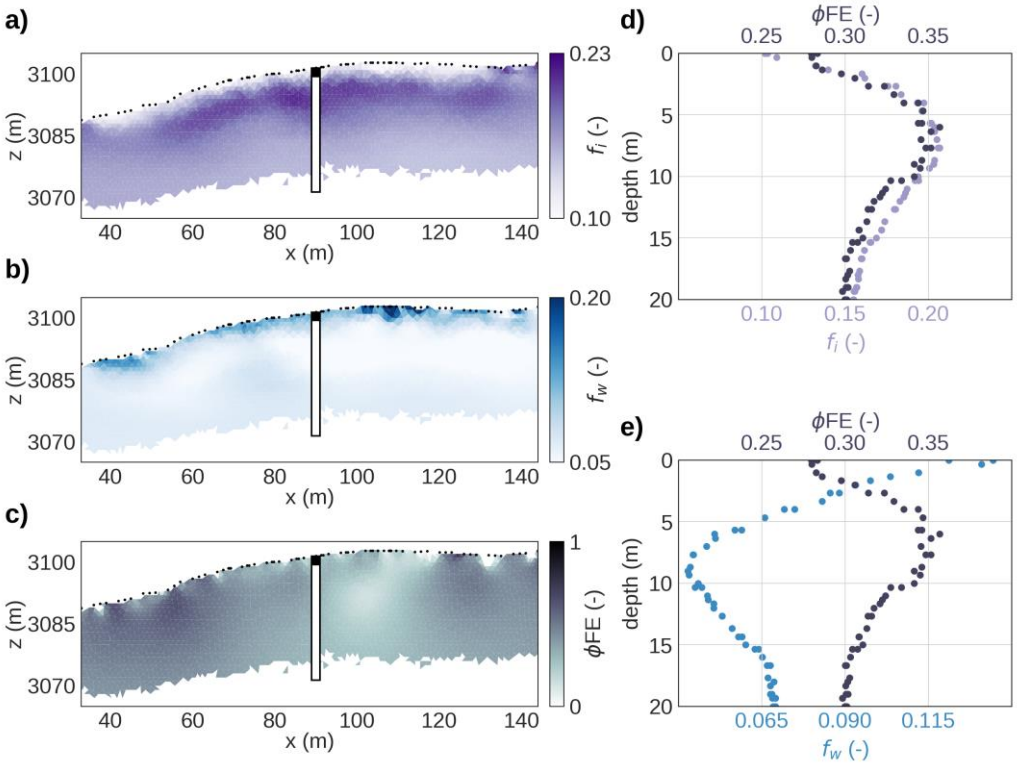

Figure 8: (a-c) Calculated ϕFE for the phase of the complex resistivity imaging results between 75 Hz and 0.5 Hz and visualized for the whole tomogram for the SIP monitoring profile (between profile meter 33 and 141) and comparison with water and ice content estimates from PJI results. (d) Vertical 1D logs of the ϕFE and the ice content and (e) water content at the borehole location.

3.4 Temporal changes in the SIP results

In Figure 9, we show the temporal evolution in borehole temperatures and the complex resistivity at different frequencies (0.5, 7.5, 25 and 75 Hz) extracted for the borehole location at different depths. During the 2-years-monitoring period, we observe that complex resistivity results mainly follow the thermal evolution, but with distinct differences between the two years. Freezing started in both years (2019 and 2020) in November, with the advance of the freezing front reflected in a decrease in temperature and an accelerated increase of the electrical parameters. The winter 2020/21 was much colder than 2019/20, which is represented by ~ two times higher ρ', similar $\phi_{0.5}$ and more than three times higher $\Delta\phi_{75}$ values in January 2021 compared to January 2020. Borehole temperatures, ρ' and ϕ reached their minimum and maximum values, respectively, between January and March 2021 ($T = -5\,°C, \rho' = 6.8\ k\Omega m$, $\phi_{0.5} = 60$ mrad, $\phi_{7.5} = 180$ mrad, $\phi_{25} = 450$ mrad, $\phi_{75} = 2000$ mrad). During spring 2021 (April-June), a steady increase in shallow borehole temperatures lead to seasonal ice melt in the uppermost layer and a small decrease in shallow electrical parameters. An abrupt increase in subsurface temperatures at the end of June 2021 is reflected in a decrease of 30 % in ρ', a decrease of 85 % in $\phi_{0.5}$ and a decrease of 90 % in ϕ_{75}. Between March and June 2020, no SIP measurements were conducted. During summer 2021, we observe smaller shallow absolute ϕ values

compared to the summer period in 2020, which can be explained by a higher VWC observed in summer 2021 than in summer 2020 (i.e., Fig. 2).

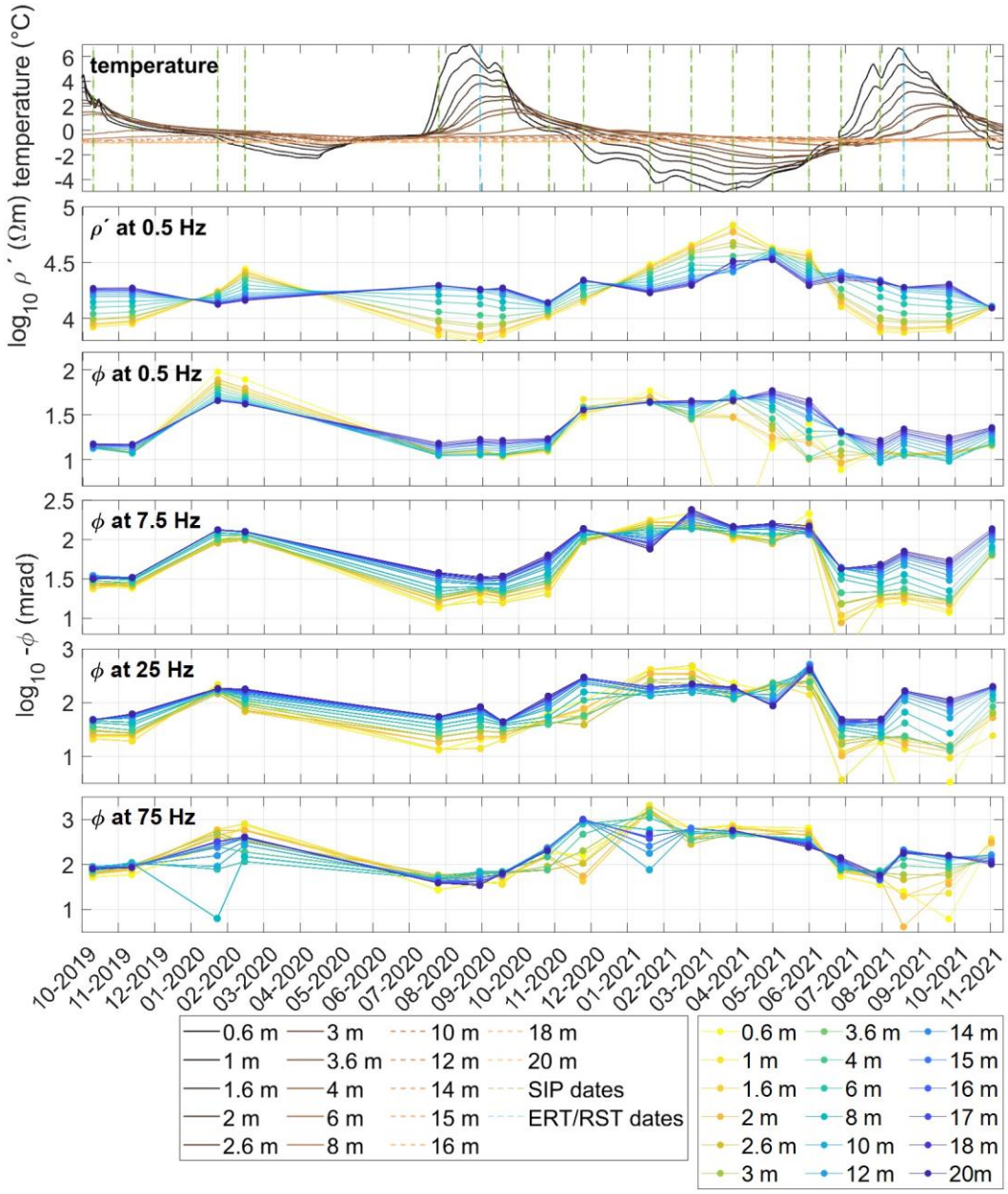

Figure 9: Comparison of borehole temperatures with complex resistivity results at different frequencies (0.5, 7.5, 25, 75 Hz) extracted at borehole position in the borehole temperature sensor depths.

3.5 Complex resistivity – temperature relationship

Fig. 10 presents the complex resistivity (ρ^*) data extracted from the SIPM inversion results at the borehole location for 4 frequencies and a comparison to the borehole temperatures (T). The T-ρ^* relationship is shown for two material compositions: debris (Fig. 10a) and bedrock (Fig. 10b) with the transition between debris and bedrock at the borehole location estimated at a depth of 1.2 m (for further details see Appendix B). The T-ρ^* was fitted for each frequency using a linear model for positive temperatures and an exponential model for subzero temperatures with the coefficients of determination obtained for the two regions and different frequencies summarized in Table D1 of Appendix D.

For unfrozen conditions, we observe that ρ' and absolute ϕ values are similar for debris and bedrock and show a linear increase in both parameters with decreasing but still positive temperature. The increase is higher for ρ' compared to ϕ. Additionally, ρ' and ϕ values are higher at 75 Hz than at 0.5 Hz (with a difference between them of $700\ \Omega$m and 50 mrad).

Below the freezing point and for both material compositions, ρ' and absolute ϕ increase exponentially with decreasing temperatures, with the highest absolute ϕ and lower ρ' values observed at 75 Hz compared to 0.5 Hz. The frequency effect in ϕ at -1 °C is different for debris and bedrock with a pronounced increase in ϕ for the debris (310 mrad) resolved for data at 0.5 and 75 Hz. Such high ϕFE reflects the expected high ice contents in winter periods in the small to coarse blocks found at the surface. Accordingly, we observe a modest change in the phase values (70 mrad) for the bedrock, where we have lower porosity and, thus, also lower ice contents. These results correspond to the laboratory results in Fig. 7, indicating that ϕFE is higher for loose sediment at subfreezing temperatures.

In the freeze-thaw transition processes, hysteresis effects are often observed also at the field-scale as shown by Mollaret et al. (2019) and Wu et al. (2013). In Fig. 10c we present the seasonal cycle at shallow depths (within the debris layer), where freezing and thawing processes can be distinguished in ρ' and ϕ at 7.5 Hz (which represents the sensitive frequency) and for the ϕFE calculated between 0.5 and 75 Hz. Similar to the laboratory results, we also observe at the field-scale lower ρ' and ϕ values and slightly lower ϕFE during freezing (from October to January) than during thawing (from May to July) which is related to the difference in liquid water content for the two processes. While ρ', ϕ and ϕFE values are small in October/November, an increase occurred in January-February with peak values detected between February and May. During snow melt in May-June, the ρ', ϕ and ϕFE values drop abruptly with the absolute phase at 7.5 Hz decreasing from 100 to 10 mrad and the ϕFE falling below 0.25 as soon as water content increases. The zero-curtain effect could not be observed during the phase change as the temporal resolution of the monitoring was too low during this period.

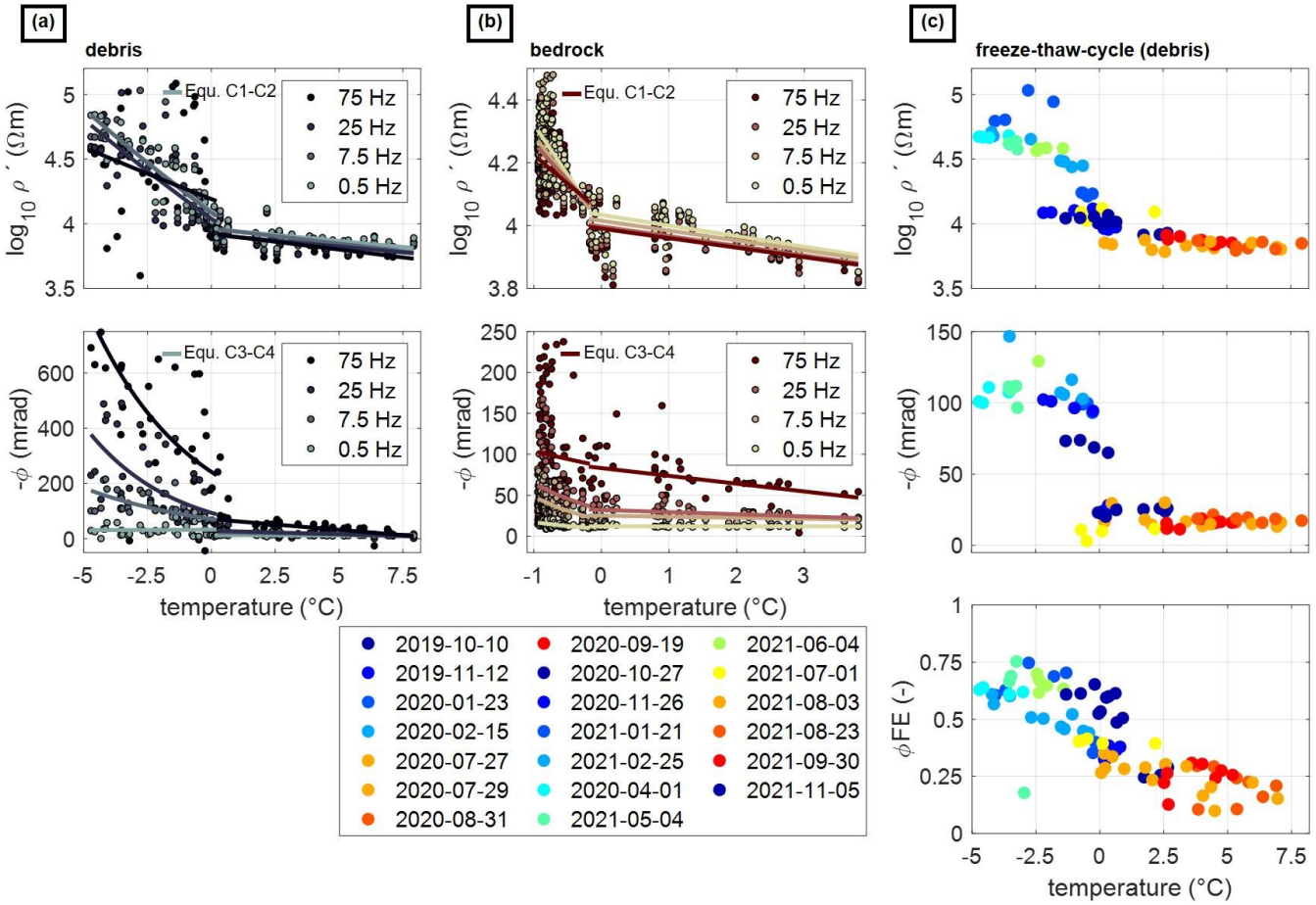

Figure 10: Temperature dependence of the complex resistivity at different frequencies (0.5. 7.5, 25 and 75 Hz) obtained from 2-years SIP monitoring data extracted at borehole location for all temperature sensor depths down to 20 m: a) debris (<1.2 m depth), b) bedrock >1.2 m depth). The data were fitted for each frequency using a linear model for positive temperatures and an exponential model for subzero temperatures according to equations D1-D4 of Appendix D. In (c) we show the temperature-resistivity relation, temperature-phase relation at 7.5 Hz and the temperature-phase frequency effect relation for the debris for all available dates.

4 Discussion

4.1 Reliability of SIP monitoring measurements

We investigated the subsurface polarization properties for both seasonal and inter-annual changes along a transect located in a mountain permafrost environment in the Italian Alps. Our monitoring results reveal an overall increase in resistivity and phase of the complex resistivity during the winter months. However, such an increase is also observed at larger depths (i.e., > 10 m) where expected changes in temperature, water content and ice content are small. High phase readings in winter are partly due to low current densities injected in frozen terrain covered by snow, resulting in low signal-to-noise-ratios (S/N), and partly also due to parasitic electromagnetic fields in the measurements. While inductive coupling effects can be neglected in our case,

as the high resistivity of the substrate shifts inductive coupling to higher frequencies mainly affecting data in the kHz range, parasitic capacitive coupling (PCC) need to be considered due to current leakage associated to the high impedance of soil, electrodes and cables (Binley et al. 2005; Flores Orozco et al., 2018; Ingeman-Nielsen, 2006; Kemna et al. 2012; Zimmerman et al., 2008). Especially at frequencies >100 Hz, significant phase errors occur due to PCC effects among electronic components and wires within the instrument making the reliability of the acquired phase spectra in different SIP studies uncertain (Wang and Slater, 2019). PCC effects create pathways through which leakage currents can flow from high to low potential surfaces or conductors as described for field measurements by Dahlin and Leroux (2012). Ingeman-Nielsen (2006) proposed an electric circuit model in order to describe the effects of electrode contact resistance and PCC on complex resistivity measurements and found that an increase in frequency, dipole size, contact resistance or wire-to-ground capacitance leads to an increase in phase errors. Wang and Slater (2019) developed a model for the prediction of high frequency phase errors at the lab scale and suggested a phase correction method that results in accurate SIP data up to 20 kHz. Such studies highlight that an increase in phase values with increasing frequency observed within our study does not automatically indicate a high ice content; but can also be related to PCC effects. Accurate SIP measurements at high frequencies are needed in order to extend the information on polarization mechanisms at high frequencies such as the polarization of ice, thus, care has to be taken in the quantification and removal of such phase errors.

4.1.1 Electric circuit experiments

To quantitatively assess the effect of a high sample resistance and PCC on SIP measurements and examine the accuracy of the DAS-1 measurement device in our SIP monitoring measurements, we built an electric circuit using commercial resistors and capacitors with known values (see Fig. 11) as suggested by Revil and Skold (2011) and performed measurements with the DAS-1 field device and the Portable Spectral Induced Polarization (PSIP) laboratory unit (Ontash & Ermac Inc., NJ). Coaxial cables were used to connect the circuit and instrument ports reducing cross talking, similar as for field conditions. We first collected impedance measurements on a resistor network with varying resistances from $10\ \Omega$ to $15\ k\Omega$ (Fig. 11a). For the PSIP instrument we observe high accuracy for both magnitude and phase measurements, where the measured values confirm the theoretical response for all resistors. The SIP field instrument proves high accuracy from 0.1 to 75 Hz for resistances up to $1\ k\Omega$, which demonstrates that coupling effects of the device and the cables can be neglected. If R exceeds $1\ k\Omega$, the magnitude of the impedance is underestimated and the phase response increases with frequency due to the capacitive load of the amplifiers similar to Zimmerman et al. (2008). Above 100 Hz, phase errors of 10 mrad occur, wherefore these measurement frequencies were not considered in our SIP monitoring analysis. In Fig. 11b we show impedance measurements of the PSIP and DAS-1 devices of a known resistance in parallel to a known capacitance. At low frequencies and resistances both devices show phase errors less than 0.5 %. At frequencies above 100 Hz, phase values strongly deviate from the theoretical response, highlighting the need for correction methods such as presented by Wang and Slater (2019) when modelling and interpreting phase measurements at higher frequencies. For measurements above 10 Hz, a sudden decrease in phase values leads to an underestimation of the theoretical response of the DAS-1 measurements, which is consistently observed for all measurements. Yet, the phase frequency effect is still a stable measure with phase frequency errors smaller than 4 % for resistances < $1\ k\Omega$

for the laboratory and the field devices. Concerning our SIP monitoring measurements, such analysis shows that phase errors due to PCC of the instrumentation or cables can be neglected for frequencies between 0.1 and 75 Hz. However, if sample resistances exceed 1 $k\Omega$, as could be the case for winter measurements, phase errors increase leading to a high data uncertainty. Nonetheless, freeze-thaw transitions are well-resolved and reveal consistent seasonal trends, hence, our analysis focuses on the summer period as well as the freezing and thawing period. For a detailed interpretation of winter SIP measurements, future studies should consider the simulation of the effect of high contact impedances of current and potential electrodes, which additionally increases phase errors as pointed out by Ingemann-Nielsen (2006).

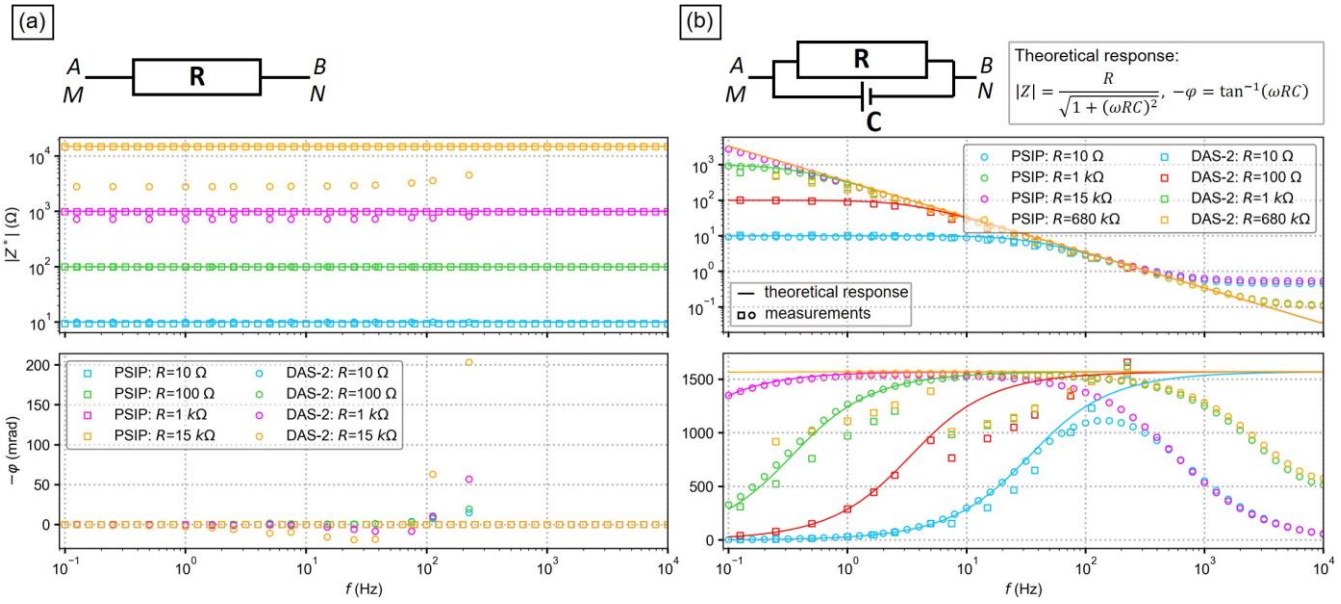

Figure 11: Test of the phase accuracy of the SIP measurement device used in our field surveys. We show the measured (with the PSIP lab device and the DAS-1 field device) and calculated magnitude and phase response of a resistor network with varying resistances (a) and for a known resistance in parallel to a known capacitance ($C = 470\ \mu F$) (b).

4.2 Temporal variability of the phase frequency effect and unfrozen water content

Our results suggest a correlation between ice content and the increase in the frequency dependence of the polarization, in particular the resistivity phase values. Frolov (1973) showed that the electrical properties of the frozen soil are determined by the specific surface area of the soil, the ice and unfrozen water content. Figure 12a illustrates how the ϕFE changes as a function of time and depth at the borehole location with a comparison to volumetric water content (VWC) (12b) and unfrozen water content (UWC) (12c) variations during freeze-thaw processes.

As discussed above, the ϕFE shows up to 3 times higher values than those for the summer period due to the high sample resistance leading to high phase errors and hence, data uncertainty in winter measurements. Nonetheless, freeze-thaw transitions are well-resolved and reveal consistent seasonal trends for the parameters ϕFE, VWC and UWC as observed in Fig

12. Supercooling leads to a higher unfrozen/volumetric water content and lower ϕFE compared with thawing processes at the same temperature with differences of $\Delta VWC \approx 6\ \%$ and $\Delta\phi FE \approx 0.15$ for the two processes. During the freezing period in 2019, measured VWC is high until January 2020 (measured VWC=18%), while in the subsequent years water contents drop to their yearly minimum (VWC=8%) already in November. The ϕFE follows the same trend. The drop in water content due to ice formation is always accompanied by an increase in the ϕFE. Similar to our study, Wu et al. (2017) observed an increase in phase at 1 Hz between -2 and -4 °C in saline permafrost, which they relate to supercooling effects and the initiation of ice nucleation. In spring (beginning of July 2020/ end of June 2021), the shallow ϕFE values decrease abruptly ($\Delta\phi FE \sim 0.17$) as soon as VWC increases to its maximum (17-30%). In late summer and autumn, we observe a steady decrease in water content and increase in phase frequency effect, with decreasing air and subsurface temperatures.

Although measured VWC and those derived from ρ' show similar trends and lie in the same range, we observe wetter conditions at the beginning of snow melt which only affect the measured VWC. This can be attributed to the different volumes of investigation from electrical measurements and the in-situ sensor, as well as possible inaccuracies in the calibration of the petrophysical model. Additionally, water content estimates can be improved by taking into account surface conductivity from SIP studies. Eq. 8 used to calculate VWC neglects surface conduction; however, this cannot be neglected in the presence of ice within the subsurface, as we observe an increase in polarization (ρ'' and ϕ) in our laboratory and field data. We note here that the imaginary conductivity is considered as a direct measure of surface conductivity (e.g., Binley and Slater, 2020); thus, the parameters ρ'' and ϕ can also be used as approximations to understand the spatio-temporal variations in surface conductivity. Duvillard et al. (2018) performed a 3D-survey at a rock glacier in France and analyzed the slope of the trend in normalized chargeability as a function of conductivity data, with the authors suggesting that the ratio ($R = \frac{\lambda}{B}$) between the apparent mobility of counterions for polarization (λ) and the intrinsic mobility of counterions in the Stern and diffuse layers (B) with R between $R = 8 \cdot 10^{-2}$ and $R = 12 \cdot 10^{-2}$ indicates that surface conduction dominates over other mechanisms. However, such relationship focuses only on the low-frequency response of the signatures and does not take into account the surface conductivity of ice. Our results reveal a significant frequency dependence of the polarization, especially between the low (< 7.5 Hz) and high frequencies, which we quantify through the ϕFE. Accordingly, we cannot apply the equation proposed for the temperature dependence in freezing conditions by Duvillard et al. (2021) and assume that electrolytic conduction dominates in our data, especially for measurements above 7.5 Hz. In case of time-domain measurements, such as those conducted by Duvillard et al. (2018), the parameter retrieved is the normalized chargeability, which is an average value that accounts for the polarization over the frequency-bandwidth recovered through the sampling of the decay-curve. Accordingly, data collected in time-domain with long pulses (1 s and 1.5 s) as presented in the studies of Duvillard et al. (2018) and Duvillard et al. (2021) will relate rather to processes taking place at solid-fluid EDL (as observed in our case <7.5 Hz) and not to the polarization of ice observed in our lab and field measurements at higher frequencies. Hence, SIP data and the representation of the SIP ϕFE could therefore help to assess changes in the surface conductivity accompanying temperature changes and to

delineate spatial changes in water and ice content in monitoring and mapping applications as demonstrated above and in the study by Maierhofer et al. (2022).

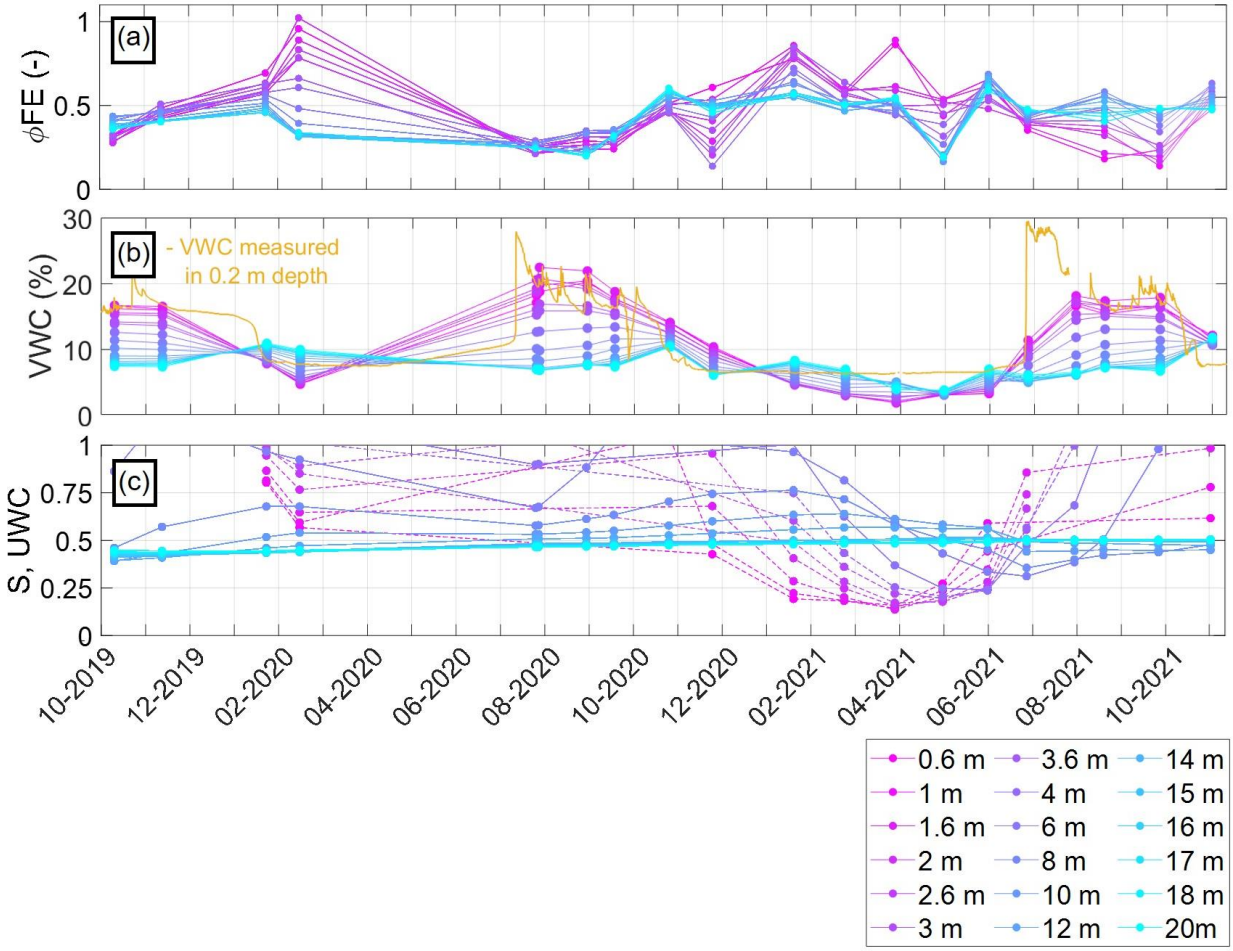

Figure 12: Temporal changes in (a) ϕFE, (b) measured and estimated volumetric water content (VWC) and (c) unfrozen water content (UWC) at the borehole location at various depths (0.6 - 20 m). The cementation exponent was estimated for a given measurement of VWC (baseline date in October 2019) within the debris layer ($\Phi = 0.6$). Porosity, fluid resistivity ($\rho_\omega = 220\ \Omega_m$), cementation exponent ($m = 2.2$) and saturation exponent ($n = 2$) were kept constant over time and VWC was calculated using Equations 7, 9 and 10.To obtain the UWC (Equ. 12), the parameter b was fitted for each depth according to the exponential behavior of the corresponding resistivity data at 0.5 Hz using Equ. 11 with $\rho_0 = 9.331\ \Omega_m$ and $T_F = -0.17\ °C$.

4.3 Spatio-temporal variability of the phase frequency effect

Pogliotti et al. (2015) found a pronounced spatial variability in the active layer thickness at the two boreholes in Cervinia Cime Bianche (cf. table 1) and argue that the difference can be related to contrasting water contents and varying surface and

subsurface conditions in terms of weathering and fracturing of the bedrock. They suggest a higher ice content in the SBH compared to the DBH, which was further supported by PJI results of Mollaret et al. (2020) indicating ice contents of up to 10 % at the DBH, and up to 17 % at the SBH. Additionally, our results show (c.f., Fig. 4) an overall shallower uppermost layer in the northeast of the study site (1-2 m difference to southwest) with lower ρ' at depth close to the DBH compared to the SBH.

While Fig. 8 and Fig. 12 demonstrate a clear relation of the ϕFE and the PJI-estimated ice-content, as well as consistent temporal changes in ϕFE at the borehole position, Fig. 13 evaluates the applicability of the proposed parameter for spatio-temporal changes across the entire imaging plane. Fig. 13a shows the resolved ϕFE along the SIPM profile and the computed annual changes in ϕFE between August 2020 and August 2022, and Fig. 13c,d compare the ϕFE values at the borehole position with ground temperature readings of both boreholes. Both, the distribution with depth as well as the interannual differences show a consistent pattern between ϕFE and borehole temperatures. At the borehole location, we observe for all three dates lower ϕFE (< 0.35) in the unfrozen active layer compared to zones at > 5 m depth related to the permafrost body with ϕFE values ranging from 0.35 to 0.45. From numerical modelling (not shown) we found that an electrode separation of 3 m with dipole lengths of 3 and 12 m were small enough to delineate the transition between the thawed active layer and the permafrost using the ϕFE. Previous geophysical investigations along the ERT/RST monitoring profile in August 2017 report low seismic P-wave velocities of $< 1000\ ms^{-1}$ and low electrical resistivities of $< 10\ k\Omega m$ within the uppermost 4-5 m thick layer and intermediate electrical resistivities ($10 - 50\ k\Omega m$) and high seismic velocities ($2000 - 5000\ ms^{-1}$) for the permafrost zone below (Mollaret et al., 2020). PJI results of the seismic and electrical data yielded ice contents of ~15 % within the permafrost body at the SBH, where also the ϕFE shows high values. In accordance with borehole temperatures, Figure 13a also reveals clearly lower ϕFE in the permafrost at depths between 8 and 15 m in 2020 ($\phi FE \approx 0.36$) compared to the colder year 2022 with ϕFE values in the range of 0.45 (see yellow box in Fig. 13a). Hence, our results suggest that inter-annual temperature changes of ≈0.2 °C at depth can be resolved by the change of 0.05 in the ϕFE, implying a high sensitivity of SIPM to small changes in temperature that might not be resolved through ERT monitoring alone. Below 20 m, we assign low credibility to the ϕFE values due to large DOI values (i.e.,> 0.2) and low sensitivity in the computed images.

The general tendency of ϕFE for the entire imaging plane of the SIPM profile is similar to that of the borehole location (Fig. 13b and 13c), however, the lateral heterogeneity is more pronounced than a vertically homogeneous pattern. In the northern part of the SIPM profile (i.e., between 0-30 m), with lowest ρ' values and small ϕFE for all dates, also ϕFE changes are the smallest during the SIP monitoring period, with a slight decrease in ϕFE (ϕFE difference ≈ -0.1) between August 2020 and August 2021 and an increase between 2021 and 2022 (ϕFE difference ~ 0.1). Due to the low ϕFE and ρ' values at all depths in the north of the study site (see, e.g. Fig. 4), we interpret this part of the monitoring profile as an area of low ice contents. The highest ρ' and ϕFE values are observed in the south between 140- and 189- meters profile length, where the surface is dominated by the coarsest blocks within the study site. Here, we find a consistent increase in ϕFE over the 2 years with positive

ϕFE differences of ≈0.3 between 2020 and 2022 indicating a high change in temperature/ice content within this part of the SIPM profile. Between profile meter 40 and 60 as well as between 90 and 115 m, two anomalies are resolved, characterized by not consistent changes in the ϕFE during the SIP monitoring period. Such ϕFE anomaly corresponds to high water contents resolved from PJI (c.f. Fig. 8; Fig. C1). Between 90 and 115 m, the surface cover is fine-grained and consists of silt, soil and vegetation and revealed the highest water content, as well as small $\rho'$and ϕFE values. While the permafrost body is generally assumed to be completely frozen for consecutive years with only small ice content changes at depth, strong spatio-temporal dynamics in the ϕFE at depth need to be considered with caution, as the data are inverted independently for measurements at different frequencies and time-lapses, and thus, may be subject to uncertainties associated to inversions with different regularization, sensitivity and contrasts. Such uncertainties could be reduced by the simultaneous inversion of SIP data measured over a range of frequencies (e.g. Günther and Martin, 2016; Kemna et al., 2014b; Son et al., 2007) and the inclusion of a spatio-temporal constraint. Yet, the small changes in temperature (0.2 K) observed in the borehole, demonstrate that there is a change at depth, which seems to be captured with the ϕFE. Whether the magnitude of the ϕFE is biased by the smoothness constraint inversion, is something that needs to be further explored in future studies.

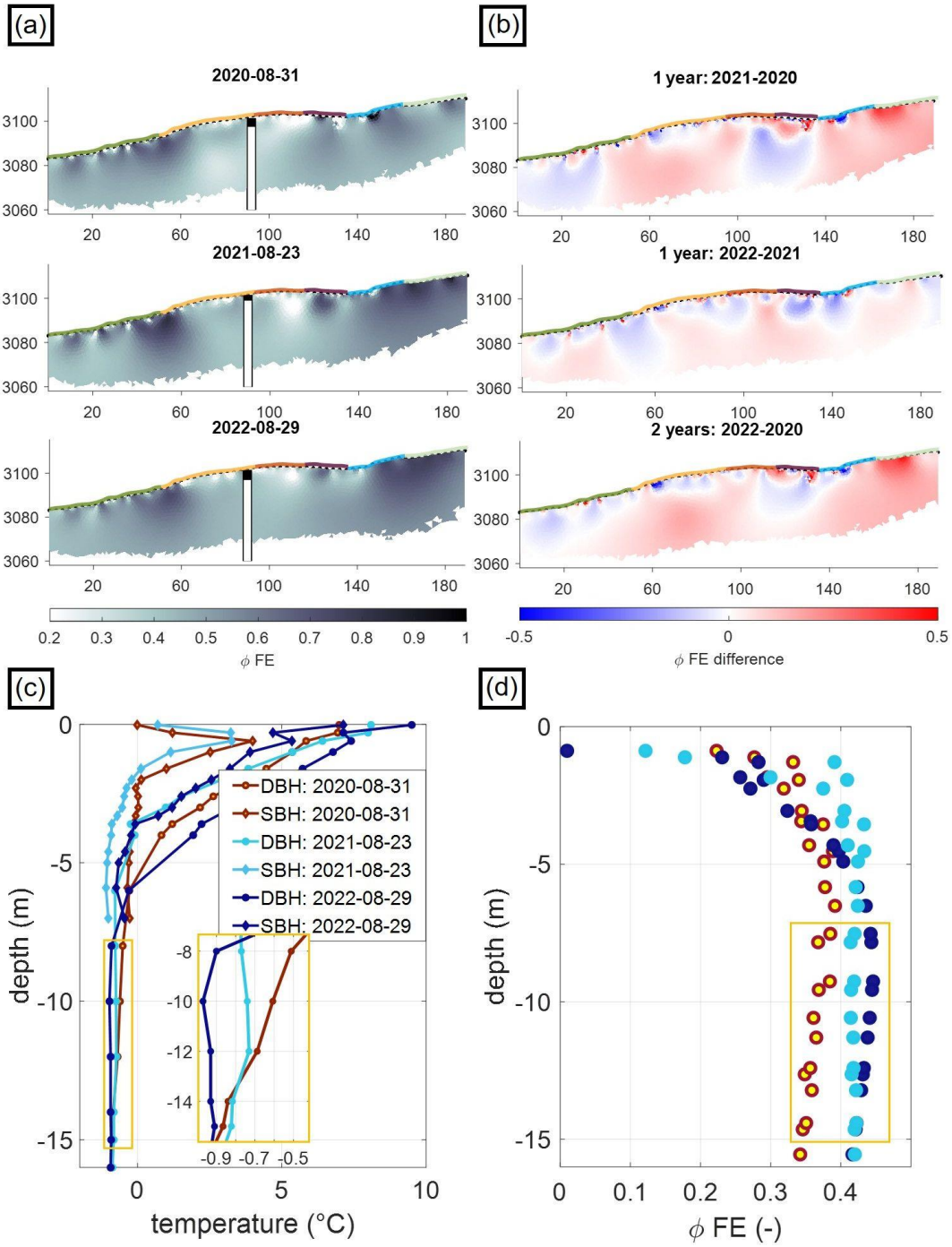

Figure 13: (a) The phase frequency effect (ϕFE) and (b) the difference in ϕFE (i.e., $\phi FE\ difference = \phi FE\ Aug22 - \phi FE\ Aug20$) is visualized between August 2020 and August 2022 for the entire imaging plane (borehole position and thaw depths are highlighted). (c) Borehole temperature data of SBH and DBH and the (d) ϕFE extracted at the borehole position for the dates of the respective SIP measurements.

4.4 Comparison of the phase frequency effect and PJI ice and water content estimations

Our analysis based on field and laboratory data suggests that temperature, water and ice contents are dominant factors controlling the frequency dependence of the SIP data throughout the freeze-thaw transition and show a high potential for an improvement in the estimation of these volumetric fractions within the subsurface. The frequency-dependent electrical properties of ice have been studied in the laboratory for pure ice, as well as for frozen solid rock and sediment samples (e.g. Auty and Cole, 1952; Bittelli et al., 2004; Grimm et al., 2010; Limbrock and Kemna, 2022) and at the field-scale (e.g. Grimm and Stillman, 2015; Mudler et al., 2022) revealing the temperature-dependent relaxation behaviour of ice (Auty and Cole, 1552) in the kHz range. By fitting a two-component Cole-Cole model to the SIP data, either for single laboratory measurements (Limbrock and Kemna, 2022) or within a 2-D inversion for field data, Mudler et al. (2022) separated the different polarization responses and estimated subsurface ice content using an existing two-component complex resistivity model of frozen soil considering the ice relaxation as the dominant process. However, such broadband spectral induced polarization measurement device (i.e., the Chameleon-2 used in the study of Mudler et al., 2022) is still not suited for monitoring and cannot be used to perform an extensive mapping as presented here. Considering that field-SIP devices are often limited in the frequency range and do not capture the ice relaxation peak, we cannot use petrophysical models linking relaxation parameters and ice content nor the fitting of Cole-Cole parameters. Instead, we propose the ϕFE, which has been revealed consistent to other data such as temperature and water content changes as discussed above. Hence, the approach presented here and the ϕFE parameter suggested might be applicable to other monitoring studies and surveys conducted with electrical devices available at the market but limited in the frequency range (for example the LIPPMANN and the Geotom measurement devices, which can collect IP measurements between 0.2 and 30 Hz). Ice content has not been directly quantified at the study area, hindering a direct comparison between ϕFE and this key parameter. The only information about the ice-content at the site has been presented by Mollaret et al. (2020) through PJI of data collected in the ERT/RST profile. We have seen that at the borehole location (see Fig. 8), ϕFE and PJI-estimated ice content are strongly correlated. In this regard, the ϕFE could be an initial way to incorporate SIP information into the 4PM, and improve the estimation of ice-content in the PJI.

Fig. 14 evaluates the correlation between the ϕFE and the ice and water contents estimated from the PJI for selected zones of interest (ZOIs) in different parts of the tomogram and for depths representative for the active layer and the permafrost body. The results show that a specific relationship, such as observed at the borehole location, is not observed in all regions of the tomogram. High ϕFE values in the permafrost body mostly coincide with high ice contents and low water contents and vice versa; however, it is not observed in all ZOIs, for instance in ZOI4 linked to fine-grained surface material . Additionally, ϕFE fluctuations within the active layer are high and ϕFE values are in the range of the permafrost body for some of these ZOIs in the active layer. Such variations in the active layer could be minimized in the future by regularization strategies as for example the minimal gradient support (Blascheck et al., 2008), which permits to solve for sharp contrasts between interfaces, and still warranty smooth variations within the different zones. Also, further studies should investigate the regularizations across time

and space dimensions to enhance the consistency between the resolved electrical models and improve the quantitative meaning of the ϕFE.

Differences observed in Fig. 14 between the ϕFE and PJI-derived ice contents at depth might indicate that ice contents might be overestimated in some areas due to the anisotropic smoothness constraint inversion or the insensitivity of SRT and ERT to possible fractures, so that lateral changes in ice content are not resolved. As mentioned above, the PJI is strongly controlled by the porosity model defined as a start model for the inversion (see, e.g. Steiner et al., 2021 for a discussion) and the gradient model forces a lateral smoothness in the parameters, which might not be present at the site. Such lateral variations will be better resolved in the SIP imaging and likely better retrieved in the frequency dependence. Additionally, Maierhofer et al. (2022) demonstrated that surface conduction changes spatially, with large polarization (σ'') associated to ice-rich areas (even at low frequencies, due to EDL polarization at the ice-water interface). In addition, our results (see Fig. 5 and Fig. 9) reveal temporal and spatial changes int surface conductivity, with ρ'' and ϕ changing across different positions of the profile (geological changes) and different seasons. The inclusion of a constant value for the surface conduction improves the overall ice content estimations based on the PJI (e.g., Mollaret et al., 2020), yet, the chosen value is only representative for pure ice, where variations due to a mixture of ice, sediment and rock are ignored. To obtain reliable petrophysical parameters based on a PJI, the spatially and temporally varying surface conduction as observed in our SIP results needs to be considered additionally.

Figure 14 also evidences an over-estimation of the ice-content in the active layer through the PJI. The occurrence of non-zero ice content estimates in regions where they are unlikely, such as in areas where temperatures are positive, have also been reported by Pellet et al. (2016) and Wagner et al. (2019), who proposed and implemented physical constraints on water content (based on soil moisture measurements) or temperature-dependent constraints on ice occurrence during inversion. However, such ice constraints are limited to sparsely distributed point locations and might bias the constraints used in the inversions, for those areas without information. Fig. 14 shows that the minimal f_i is about 10%, even for the ZOI retrieved from the AL. This problem can be resolved by fixing a spatial constraint with an ice-content of 0% in the active layer, yet such an inversion would require exact information about the geometry of the active layer.

The quantitative interpretation of ϕFE is likely still open to debate; however, its applicability is supported in our study through the analysis of independent measurements in well-controlled experiments conducted in the laboratory (Fig. 6 and Fig. 7). These analyses reveal a clear distinction in the polarization response between unfrozen and frozen states and a significant frequency dependence in the absolute ϕ values with decreasing temperature, which in turn is related to the well-known temperature-dependent relaxation behaviour of ice (Auty and Cole, 1952) with the full spectrum presented in the Appendix B. Laboratory and field results reveal that between 5 and 8 Hz an inflection point between the low polarization response at low frequencies associated to the polarization of grain-water interfaces and the increase in the response at high frequencies exist due to the polarization of ice. Such an inflection point depends on the texture of the rock as well as the ice content (and temperature) as evidenced in our laboratory measurements. Additionally, at temperatures < 0 °C, a higher increase in absolute ϕ values for the loose sediment sample and the debris compared to the solid rock sample and the bedrock suggests a correlation of ϕ with ice.

Even though a similar behaviour in the polarization during freezing and thawing cycles is observed for laboratory and field data, the increase in absolute phase is smaller for laboratory data (as shown for Fig. 7) due to less sources of noise within the laboratory. Additionally, we observe large contrasts along the SIP monitoring profile with large variations due to changes in porosity such as fractures at depth or fine-grained to coarse blocky debris at the surface. These changes play a big role in the inversion of the field data, especially when inverted at different frequencies. Hence, future investigations should consider investigating the influence of small heterogeneities within the debris layer by using small electrode spacings. We also note here that the ϕFE needs to be analysed for measurements at other sites, corresponding to different lithology, porosity and ice content. Moreover, other polarization processes occurring at higher frequencies, for example related to high clay content, metallic minerals or peat within the subsurface, would also influence the ϕFE and need to be addressed in future studies. In this regard, the ϕFE offers so far rather qualitative information about the geometry and temporal changes in areas rich in ice. Further studies might attempt to include such information at least as a spatial-constraint within the PJI.

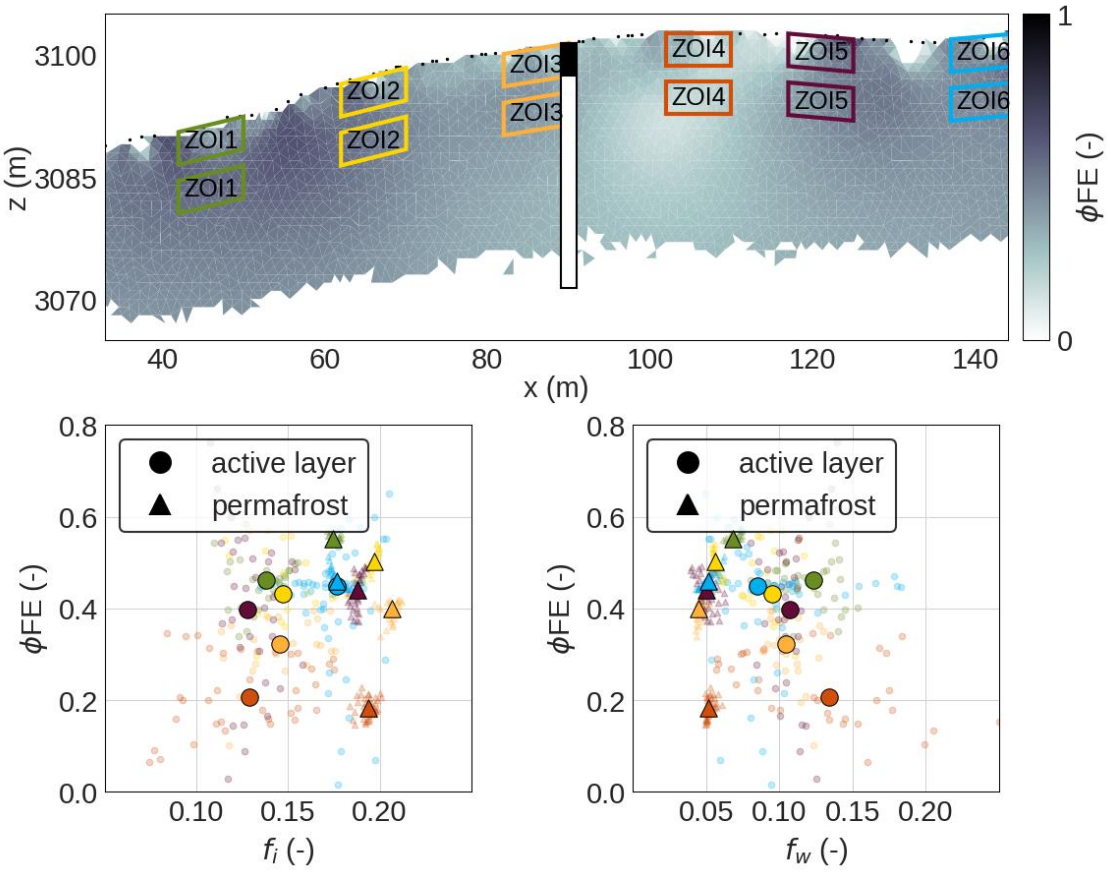

Figure 14: Correlation between PJI-derived ice and water content estimates and the phase frequency effect for selected zones of interest (ZOIs) within the active layer and the permafrost body along the SIP monitoring profile.

Additional investigations are needed to find a petrophysical model linking SIP parameters and ice content, where the ϕFE could be a first option. Such a model could explicitly account for surface conduction and thereby help to reduce the uncertainty in the PJI inversion. However, to that end further SIP measurements at different sites and ice content are required (Maierhofer et al., 2021).

5 Conclusions and outlook

In this study, we presented time-lapse SIP imaging data collected at a mountain permafrost site during a measurement period of 3 years. The data were obtained in the frequency domain between 0.1-75 Hz using a combination of dipole-dipole normal and reciprocal and multiple gradient protocols. Our analysis highlights clear seasonal changes in the complex resistivity images for all frequencies with an increase in late autumn and a decrease in early summer and most prominent changes at shallow depths in the active layer. Characteristic changes in polarization can be attributed either to the freezing period in autumn (September-November), before a permanent snow cover has been established, or to subsurface thawing processes in late spring and early summer (June-July), when melting snow and rain lead to a decrease in phase values. During winter, complex resistivity values increase to their maximum for all frequencies and depths, which can partly be explained by the high resistance leading to an increase in phase errors and data uncertainty. This is demonstrated within electric circuit tests in the laboratory to assess the effect of a high sample resistance and electromagnetic fields (i.e., parasitic capacitive coupling) on SIP measurements and examine the accuracy of the phase measurements collected with the field measurement device.

Complex resistivity-temperature relationships at the borehole location show a linear dependency for positive temperatures and an exponential relation for subzero temperatures with different amplitudes for different substrates (debris and bedrock). Clear hysteresis effects are observed in the freeze-thaw transition processes relating the change in polarization signals to a difference in water content for these phase changes. Supercooling effects are observed through lower complex resistivity values during freezing than during thawing, which is due to higher unfrozen water contents during freezing compared to thawing processes at the same temperature. This interpretation is confirmed by laboratory measurements on rock samples from the site, which upon freezing and thawing exhibit an absolute phase increase with decreasing temperature at higher frequencies, with the general spectral behaviour being consistent with the known polarization properties of ice.

Our analysis based on field and laboratory freeze-thaw cycles as well as on spatial patterns of the SIP behaviour in freezing conditions suggests that temperature, water and ice contents are dominant factors controlling the polarization at the frequencies measured in this study. Considering that field-SIP devices are often limited in the frequency range and might lack the possibility to recover the frequency of the polarization maximum (in our case the full process of ice relaxation) required to fit a dispersion model such as the Cole-Cole, this study focuses on the investigation of the phase frequency effect, exploiting the spectral information gained through SIP field measurements in a frequency range between 0.1-75 Hz. Yet, it is important that the frequency range in the SIP data extends above a sensitive frequency, which corresponds to an inflection point between the

low polarization values (due to the polarization of rock-water interface) and the high values associated to the polarization of ice. We propose the resistivity phase frequency-effect (ϕFE) as a proxy to discriminate between regions with no ice and regions richer in ice (i.e., also to discriminate temporal changes in ice content). Laboratory and field data show a clear exponential increase of the temperature dependence of the ϕFE during freezing and higher amplitudes for higher ice contents (i.e., in the pores of the sediment sample and within the debris layer). Inter-annual changes of the ϕFE at the field-scale are spatially heterogeneous, which is interpreted to be related to varying surface/subsurface conditions, temperature changes as well as ice and water contents along the monitoring profile. Small changes in temperature at depth can be resolved by SIP through examining changes in the ϕFE .

When comparing the phase frequency effect with ice content estimates from collocated electric and seismic data sets using the petrophysical joint inversion scheme (PJI), we observe a high consistency at the borehole location, but do not obtain the same relationship for the entire imaging plane. These inconsistencies highlight the difficulty of obtaining ice content data sets for validation, as also PJI-derived ice content estimates are based on various assumptions within the petrophysical model with inherent uncertainties. Future investigations should focus on the integration of IP data in the PJI approach as structural constraints or as additional parameter in the underlying petrophysical model for an improved estimation of the ice content with applications in different permafrost landforms. In the presence of ice within the subsurface polarization increases and thus, spatially and temporally varying surface conduction has to be considered additionally to electrolytic conduction within the PJI to obtain reliable petrophysical parameters. Thus, further investigations are needed to find a petrophysical model linking IP and ice content such as a combination of the phase frequency effect with additional laboratory studies required to link the phase frequency effect with ice contents.

Appendix A

In Table A1, we present the measurement setup for SIP data collected along the monitoring profile between October 2019 and October 2022 and additional filtering parameters.

Table A3: Filtering of SIP time lapse data – monitoring setup (electrode configuration and frequency range) and remaining quadrupoles after filtering for each measuring date

Measurement date	Electrode configuration	Frequency range (Hz)	Mean contact resistances (Ω)	Mean injected current intensities (mA)	Remaining quadrupoles after filtering, 1/0.5 Hz	Remaining quadrupoles after filtering, 75 Hz
2019-10-10	DDsk3 N&R; MGsk0-3	0.5-225; 0.1-225	24180	10.4; 9.7	671; 612	366; 550
2019-11-12	DDsk3 N&R; MGsk0-3	0.5-225; 0.25-225	22870	10.4; 9.5	670; 569	366; 473

2020-01-23	DDsk3 N&R; MGsk0-3	0.5-225; 0.1-225	110140	2.3; 1.5	183; 339	123; 164
2020-02-15	DDsk3 N&R; MGsk0-3	1-225; 0.1-225	116730	1.5; 1.1	141; 348	105; 207
2020-07-27	MGsk0-3	0.5-225	24950	10.2	685	551
2020-07-29	MGsk0-3	0.1-225	26810	9.2	605	441
2020-07-30	DDsk3 N&R	1-225	21920	10.6	699	386
2020-08-31	MGsk0-3	0.1-225	26530	10	561	399
2020-09-19	DDsk3 N&R; MGsk0-3	1, 7-225; 0.1-225	22320	9.6; 9.4	787; 618	309; 426
2020-10-27	DDsk3 N&R; MGsk0-3	0.5-225; 0.1-225	64790	3.7; 10.9	437; 571	214; 357
2020-11-26	DDsk3 N&R; MGsk0-3	1-225; 0.1-225	120170	2.2; 3.6	263; 472	203; 313
2021-01-21	DDsk3 N&R; MGsk0-3	1-112.5; 0.1-225	156630	1.1; 1.4	90; 127	100; 139
2021-02-25	MGsk0-3	0.1-225	146150	0.4	218	232
2021-04-01	DDsk3 N&R; MGsk0-3	1-112.5; 0.1-225	138090	0.7; 0.5	121; 447	107; 348
2021-05-04	DDsk3 N&R; MGsk0-3	0.5-112.5; 0.1-225	136380	0.2; 0.6	154; 294	150; 246
2021-06-04	DDsk3 N&R; MGsk0-3	0.5-225; 0.1-225	88990	1.4; 1.4	318; 358	204; 301
2021-07-01	DDsk3 N&R; MGsk0-3	0.5-225; 0.1-225	38230	6.1; 5.2	469; 375	315; 265
2021-08-03	DDsk3 N&R; MGsk0-3	1-225; 0.1-225	28080	8.8; 8.7	656; 555	364; 379
2021-08-09	DDsk3 N&R	1-225	38490	11.3	787	458
2021-08-23	DDsk3 N&R; MGsk0-3	0.1-225	32420	11.4; 9.8	588	421
2021-09-30	DDsk3 N&R; MGsk0-3	0.5-225; 0.1-225	35200	7.7; 8.5	751; 634	416; 476

2021-11-05	DDsk3 N&R; MGsk0-3	0.1-225	103160	1.9; 1.6	540	324	

Appendix B

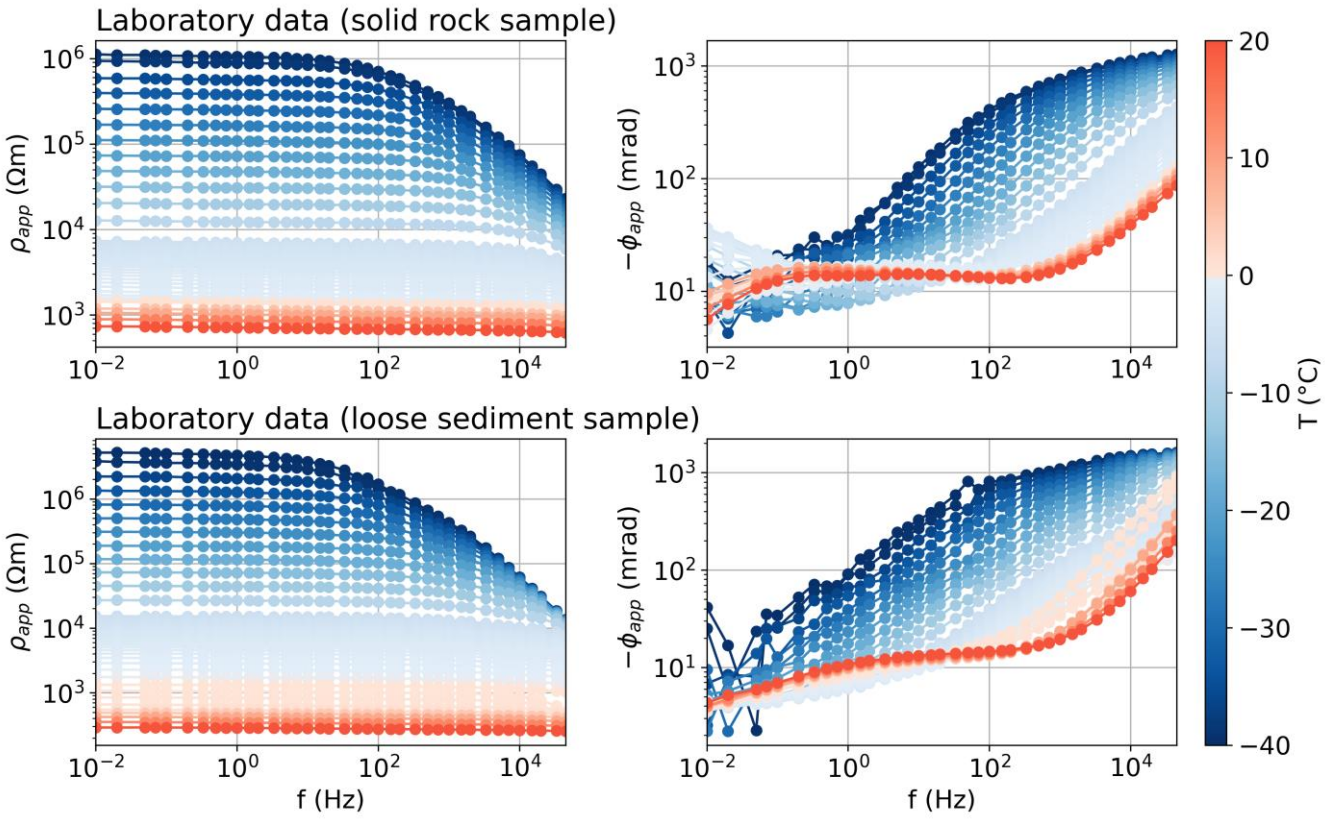

Figure B1: Broadband SIP laboratory measurements on a solid rock sample and a loose sediment sample collected at the site close to the monitoring profile. Apparent resistivity and phase values are shown in a frequency range between 10 mHz and 45 kHz during controlled freeze-thaw cycles (+20°C to -40°C to +20°C).

In Fig. B1 we show laboratory measurements performed on a cylindrical solid rock sample of 10 cm length and 3 cm diameter of amphibolite (with a porosity of 3.5 %) and a loose sediment surface sample, both collected close to the SIP monitoring profile. The electrical impedance was measured in a frequency range of 10 mHz to 45 kHz during controlled freeze-thaw cycles (+20°C to -40°C to +20°C).

Appendix C

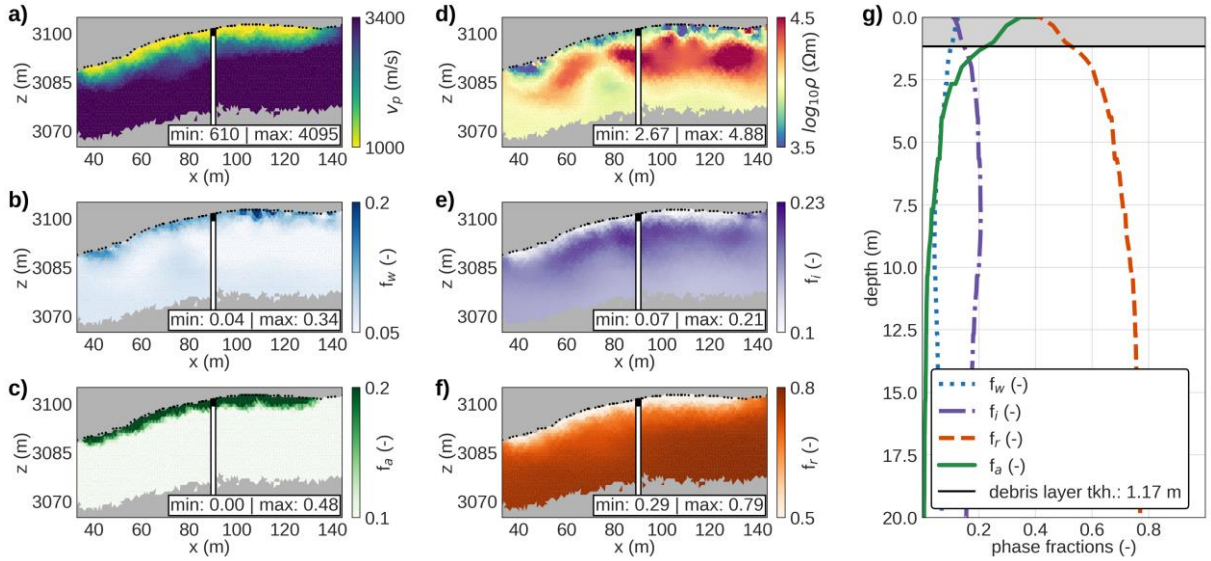

Figure C1: Petrophysical joint inversion results for August 2020. (a-f) Imaging results in terms of geophysical parameters, i.e. the seismic P-wave velocity (v_p) and electrical resistivity (ρ), and petrophysical parameters, i.e the ice, water, air and rock contents resolved through the petrophysical joint inversion. (g) Virtual 1D logs extracted from the imaging results at the borehole location and estimated debris layer thickness.

In Fig. C1 we show PJI results for seismic travel times and electrical resistivity measurements collected along the SIP monitoring profile. Differing velocities can be observed between the debris and bedrock with lowest velocities occurring in the near-surface within the porous debris layer ranging from roughly 500 to 1500 m/s, corresponding to a high air content. Maximum rock contents with a porosity of ~20% and minimum rock contents reaching a porosity of 70% are encountered in the bedrock and surface debris layer, respectively. Accordingly, the transition between debris and bedrock at the borehole location was estimated at a depth of 1.2 m by calculating the inflection point in rock content at the borehole position.

Appendix D

The complex resistivity data were fitted for each frequency using a linear model for positive temperatures and an exponential model for subzero temperatures according to

$$\rho(T) = a \cdot T + b \quad \text{(D1)}$$

$$\rho(T) = a \cdot \mathrm{e}^{(b \cdot T)} \quad \text{(D2)}$$

$$\phi(T) = a \cdot T + b \quad \text{(D3)}$$

$$\phi(T) = a \cdot \mathrm{e}^{(b \cdot T)} \quad \text{(D4)}$$

with the coefficients for different frequencies for debris and bedrock summarized in table C1.

Table D4: Coefficients for complex resistivity – temperature fits for two frequencies (0.5 and 75 Hz) and for two material compositions (debris and bedrock).

parameter	debris (0.5 Hz)	debris (75 Hz)	bedrock (0.5 Hz)	bedrock (75 Hz)
ρ (T < 0°C)	a = -0.0187	a = -0.0185	a = -0.0337	a = -0.03
	b = 3.9610	b = 3.8982	b = 4.034	b = 3.9887
ρ (T < 0°C)	a = 4.0986	a = -8.55e+03	a = 4.0076	a = -2.2639e+03
	b = -0.0351	b = -0.1589	b = -0.0757	b = -0.5124
ϕ (T > 0°C)	a = -0.209	a = -7.6766	a = 0.0173	a = -9.5084
	b = 13.1938	b = 70.7333	b = 12.0308	b = 83.1597
ϕ (T< 0°C)	a = 32.8829	a = -14.0334	a = 8.9605	a = 13.4545
	b = 0.0109	b = -176.9885	b = 0.6501	b = 8.1572

Data availability. The borehole temperature data from the ARPA office, as well as the SIP field and laboratory data that support the findings of this study are available from the corresponding author upon request and will be provided through an online data repository after acceptance of the manuscript.

Author contributions. TM, AFO and CHa designed the experimental setup, TM, ED, UMD and AFO planned and coordinated the field logistics of the installation and conduction of the monitoring measurements and ED and UMD provided further background information of the site. TM, AFO and NR processed the geophysical field data and CM helped in the preparation of a figure. JL and AK collected and processed the laboratory data. AFO, CHa, CHi and TM interpreted the geophysical signatures and CHa, AFO, NR, CHi, AK, JL and TM discussed the results. TM led the preparation of the draft and wrote the major part of the text, where CHa, AFO and Chi helped essentially, while all authors contributed actively to the intermediate and final version of the manuscript.

Acknowledgements. This study is supported by the Swiss National Science Foundation (SNSF) (project number: 200021L_1788236) and the German Research Foundation (DFG) (project number: 403089687). We are furthermore thankful to the ARPA office for providing the borehole temperature data and ARPA as well as the cable car company Cervino S.p.A for the logistical support of our research activities at the Cervinia Cime Bianche field site. We also thank Michel Isabellon, Lukas Aigner, Paolo Pogliotti, Doris Schlögelhofer, Alberto Carrera, Walter Loderer and Sarah Morard for the help in the preparation of the equipment, the installation of the geophysical monitoring profile and the collection of the geophysical monitoring data.

Competing interests. The authors declare that they have no conflict of interest.

References

Auty, R. P. and Cole, R. H.: Dielectric properties of ice and solid D2O, J. Chem. Phys., 20, 1309–1314, https://doi.org/10.1063/1.1700726, 1952.

Bazin, S., Lysdahl, A., Olaus Harstad, A., and Frauenfelder, R.: Resistivity and Induced Polarization (ERT/IP) survey for bedrock mapping in Permafrost, Svalbard, 25th Eur. Meet. Environ. Eng. Geophys. Held Near Surf. Geosci. Conf. Exhib. 2019, NSG 2019, The Hague, The Netherlands, 8–12 September 2019, 1–5, https://doi.org/10.3997/2214-4609.201902362, 2019.

Binley, A. and Kemna, A.: DC Resistivity and Induced Polarization Methods, in: Hydrogeophysics, Water Science and Technology Library book series, volume 50, edited by: Rubin, Y. and Hubbard, S. S., pp. 129–156, https://doi.org/10.1007/1-4020-3102- 5_5, 2005.

Binley, A. and Slater, L.: Resistivity and Induced Polarization: theory and Applications to the Near-Surface Earth, Cambridge, United Kingdom, New York, USA, New Delhi, India, ISBN 9781108685955, https://doi.org/10.1017/9781108685955, 2020.

Binley, A., Slater, L. D., Fukes, M., and Cassiani, G.: Relationship between spectral induced polarization and hydraulic properties of saturated and unsaturated sandstone, Water Resour. Res., 41, W12417, https://doi.org/10.1029/2005WR004202, 2005.

Binley, A., Kruschwitz, S., Lesmes, D., and Kettridge, N.: Exploiting the temperature effects on low frequency electrical spectra of sandstone: A comparison of effective diffusion path lengths, Geophysics, 75, 10–13, https://doi.org/10.1190/1.3483815, 2010.

Biskaborn, B. K., Smith, S. L., Noetzli, J., Matthes, H., Vieira, G., Streletskiy, D. A., Schoeneich, P., Romanovsky, V. E., Lewkowicz, A. G., Abramov, A., Allard, M., Boike, J., Cable, W. L., Christiansen, H. H., Delaloye, R., Diekmann, B., Drozdov, D., Etzelmüller, B., Grosse, G., Guglielmin, M., Ingeman-Nielsen, T., Isaksen, K., Ishikawa, M., Johansson, M., Johannsson, H., Joo, A., Kaverin, D., Kholodov, A., Konstantinov, P., Kröger, T., Lambiel, C., Lanckman, J. P., Luo, D., Malkova, G., Meiklejohn, I., Moskalenko, N., Oliva, M., Phillips, M., Ramos, M., Sannel, A. B. K., Sergeev, D., Seybold, C., Skryabin, P., Vasiliev, A., Wu, Q., Yoshikawa, K., Zheleznyak, M., and Lantuit, H.: Permafrost is warming at a global scale, Nat. Commun., 10, 264, https://doi.org/10.1038/s41467-018-08240-4, 2019.

Bittelli, M., Flury, M., and Roth, K.: Use of dielectric spectroscopy to estimate ice content in frozen porous media, Water Resour. Res., 40, W04212, https://doi.org/10.1029/2003WR002343, 2004.

Blaschek, R., Hördt, A. and Kemna, A.: A new sensitivity-controlled focusing regularization scheme for the inversion of induced polarization data based on the minimum gradient support, Geophysics, 73(2), pp. F45-F54, https://doi.org/10.1190/1.2824820, 2008.

Bullemer, B., Riehl, N.: Bulk and Surface Conductivity of Ice, Solid State Commun, 4, 447– 448, https://doi.org/10.1016/0038-1098(66)90325-5, 1996.

Caranti J.M. and Illingworth A.J. 1983: Frequency Dependence of the Surface Conductivity of Ice, Journal of Physical Chemistry 87, 4078–4083, doi:10.1021/j100244a016.

Coperey, A., Revil, A., Abdulsamad, F., Stutz, B., Duvillard, P. A., and Ravanel, L.: Low-Frequency Induced Polarization of Porous Media Undergoing Freezing: Preliminary Observations and Modeling, J. Geophys. Res.-Sol. Ea., 124, 4523–4544, https://doi.org/10.1029/2018JB017015, 2019.

Dahlin T., Zhou B.: Multiple-gradient array measurements for multi-channel 2D resistivity imaging, Near Surface Geophysics., vol. 4 (pg. 113-123), 2006.

Daniels, J. J., G. V. Keller, and J. J. Jacobson: Computer-assisted interpretation of electromagnetic soundings over a permafrost section, Geophysics, 41, 752 – 765, doi:10.1190/1.1440647, 1976.

Dash, J. G., Rempel, A. W., and Wettlaufer, J. S.: The physics of premelted ice and its geophysical consequences, Rev. Mod. Phys., 78, 695–741, https://doi.org/10.1103/RevModPhys.78.695, 2006.

Doetsch, J., Ingeman-Nielsen, T., Christiansen, A. V., Fiandaca, G., Auken, E., and Elberling, B.: Direct current (DC) resistivity and induced polarization (IP) monitoring of active layer dynamics at high temporal resolution, Cold Reg. Sci. Technol., 119, 16–28, https://doi.org/10.1016/j.coldregions.2015.07.002, 2015.

Duvillard, P., Magnin, F., Revil, A., Legay, A., Ravanel, L., Abdulsamad, F., and Coperey, A.: Temperature distribution in a permafrost-affected rock ridge from conductivity and induced polarization tomography, Geophys. J. Int., 225, 1207–1221, https://doi.org/10.1093/gji/ggaa597, 2021.

Duvillard, P. A., Revil, A., Qi, Y., Soueid Ahmed, A., Coperey, A., and Ravanel, L.: Three-Dimensional Electrical Conductivity and Induced Polarization Tomography of a Rock Glacier, J. Geophys. Res.-Sol. Ea., 123, 9528–9554, https://doi.org/10.1029/2018JB015965, 2018.

Etzelmüller, B., Guglielmin, M., Hauck, C., Hilbich, C., Hoelzle, M., Isaksen, K., Noetzli, J., Oliva, M., and Ramos, M.: Twenty years of European mountain permafrost dynamics – the PACE legacy, Environ. Res. Lett. 15, 10, https://doi.org/10.1088/1748-9326/abae9d, 2020.

Flores Orozco, A., Williams, K. H., Long, P. E., Hubbard, S. S., and Kemna, A.: Using complex resistivity imaging to infer biogeochemical processes associated with bioremediation of an uranium-contaminated aquifer, J. Geophys. Res.-Biogeo., 116, G03001, https://doi.org/10.1029/2010JG001591, 2011.

Flores Orozco, A., Kemna, A., and Zimmermann, E.: Data error quantification in spectral induced polarization imaging, Geophysics, 77, E227–E237, https://doi.org/10.1190/geo2010- 0194.1, 2012.

Flores Orozco, A., Williams, K. H., and Kemna, A.: Timelapse spectral induced polarization imaging of stimulated uranium bioremediation, Near Surf. Geophys., 11, 531–544, https://doi.org/10.3997/1873-0604.2013020, 2013.

Flores Orozco, A., Bücker, M., Steiner, M., and Malet, J.-P.: Complex-conductivity imaging for the understanding of landslide architecture, Eng. Geol., 243, 241–252, https://doi.org/10.1016/j.enggeo.2018.07.009, 2018.

Flores Orozco, A., Kemna, A., Binley, A., and Cassiani, G.: Analysis of time-lapse data error in complex conductivity imaging to alleviate anthropogenic noise for site characterization, Geophysics, 84, B181–B193, https://doi.org/10.1190/GEO2017-0755.1, 2019.

Frolov, A.D.: Elastic and electrical properties of frozen ground, In: Sanger and H. Hyde (Editors), Proceedings at 2nd International Conference on Permafrost (USSR contribution), National Academy of Sciences, Washington DC, pp. 307-312, 1973.

Glover, P.: What is the cementation exponent? A new interpretation, The Leading Edge, 28 (1), 82-85, 10.1190/1.3064150, 2009.

Grimm, R. E. and Stillman, D. E.: Field test of detection and characterisation of subsurface ice using broadband spectral

induced polarisation, Permafr. Periglac. Process., 26, 28–38, https://doi.org/10.1002/ppp.1833, 2015.

Guglielmin, M. and Vannuzzo, C.: Studio della distribuzione del permafrost e delle relazioni con i ghiacciai della piccola età glaciale nell'alta valtournenche (Valle d'Aosta, Italia), Atti Ticinesi di Scienze della Terra, 38, 119–127, 1995.

Günther, T. and Martin, T.: Spectral two-dimensional inversion of frequency-domain induced polarization data from a mining slag heap, J. Appl. Geophys., 135, 436–448, https://doi.org/10.1016/j.jappgeo.2016.01.008, 2016.

Harris, C., Haeberli, W., Vonder M¨uhll, D., and King, L.: Permafrost monitoring in the high mountains of Europe: the PACE Project in its global context, Permafrost Periglac., 12, 3–11, doi:10.1002/ppp.377, 2001.

Hauck, C.: Frozen ground monitoring using DC resistivity tomography, Geophys. Res. Lett., 29, 10–13, https://doi.org/10.1029/2002GL014995, 2002.

Hauck, C.: New Concepts in Geophysical Surveying and Data Interpretation for Permafrost Terrain, Permafr. Periglac. Process., 137, 131–137, https://doi.org/10.1002/ppp.1774, 2013.

Hauck, C. and Kneisel, C.: Applied geophysics in periglacial environments, Cambridge University Press, 256 pp., ISBN 9780511535628, https://doi.org/10.1017/CBO9780511535628, 2008.

Hauck, C., Böttcher, M., and Maurer, H.: A new model for estimating subsurface ice content based on combined electrical and seismic data sets, The Cryosphere, 5, 453–468, https://doi.org/10.5194/tc-5-453-2011, 2011.

Hausmann, H., Krainer, K., Brückl, E., and Mostler, W.: Internal structure and ice content of Reichenkar rock glacier (Stubai Alps, Austria) assessed by geophysical investigations, Permafr. Periglac. Process., 18, 351–367, https://doi.org/10.1002/ppp.601, 2007.

Harrington, J. S., Mozil, A., Hayashi, M., and Bentley, L. R.: Groundwater flow and storage processes in an inactive rock glacier, Hydrol. Process., 32, 3070–3088, https://doi.org/10.1002/hyp.13248, 2018.

Hilbich, C., Hauck, C., Hoelzle, M., Scherler, M., Schudel, L., Völksch, I., Vonder Mühll, D., and Mäusbacher, R.: Monitoring mountain permafrost evolution using electrical resistivity tomography: A 7-year study of seasonal, annual, and long-term variations at Schilthorn, Swiss Alps, J. Geophys. Res.-Earth, 113, F01S90, https://doi.org/10.1029/2007JF000799, 2008.

Hilbich, C.: Time-lapse refraction seismic tomography for the detection of ground ice degradation, The Cryosphere, 4, 243–259, https://doi.org/10.5194/tc-4-243-2010, 2010.

Hilbich, C., Fuss, C., and Hauck, C.: Automated time-lapse ERT for improved process analysis and monitoring of frozen ground, Permafrost Periglac., 22, 306–319, https://doi.org/10.1002/ppp.732, 2011.

Hilbich, C., Hauck, C., Mollaret, C., Wainstein, P., and Arenson, L. U.: Towards accurate quantification of ice content in permafrost of the Central Andes – Part 1: Geophysics-based estimates from three different regions, The Cryosphere, 16, 1845–1872, https://doi.org/10.5194/tc-16-1845-2022, 2022.

Hobbs, P. V.: Ice Physics, Clarendon, Oxford, 837 pp., ISBN 978- 0-19-958771-1, 1974.

Ingeman-Nielsen, T.: The effect of electrode contact resistance and capacitive coupling on complex resistivity measurements, SEG Technical Program Expanded Abstracts, 1376-1380, https://doi.org/10.1190/1.2369776, 2006

Isaksen, K., Ødegård, R. S., Etzelmüller, B., Hilbich, C., Hauck, C., Farbrot, H., Eiken, T., Hygen, H. O., and Hipp, T.:

degrading mountain permafrost in southern Norway: spatial and temporal variability of mean ground temperatures, 1999–2009, Permafrost Periglac., 22, 361–377, 2011.

Kemna, A.: Tomographic inversion of complex resistivity: Theory and application, PhD thesis, Ruhr-University of Bochum, ISBN 3-934366-92-9, 2000.

Kemna, A., Binley, A., Cassiani, G., Niederleithinger, E., Revil, A., Slater, L., Williams, K. H., Orozco, A. F., Haegel, F. H., Hördt, A., Kruschwitz, S., Leroux, V., Titov, K., and Zimmermann, E.: An overview of the spectral induced polarization method for near-surface applications, Near Surf. Geophys., 10, 453–468, https://doi.org/10.3997/1873-0604.2012027, 2012.

Kemna, A., Weigand, M., and Zimmermann, E.: Resistivity and SIP response of rocks during freezing and thawing, in: Proceedings of the 3rd International Workshop on Induced Polarization, Ile d'Oléron, France, 6–9 April 2014, https://ip.geosciences. mines-paristech.fr/s1_kemna (last access: 17 May 2022), 2014a.

Kemna, A., Huisman, J. A., Zimmermann, E., Martin, R., Zhao, Y., Treichel, A., Flores-Orozco, A., and Fechner, T.: Broadband Electrical Impedance Tomography for Subsurface Characterization Using Improved Corrections of Electromagnetic Coupling and Spectral Regularization, in: Tomography of the Earth's Crust: From Geophysical Sounding to Real-Time Monitoring, Springer, pp. 1–20 https://doi.org/10.1007/978-3-319- 04205-3_1, 2014b.

Keuschnig, M., Krautblatter, M., Hartmeyer, I., Fuss, C., and Schrott, L.: Automated Electrical Resistivity Tomography Testing for Early Warning in Unstable Permafrost Rock Walls Around Alpine Infrastructure, Permafr. Periglac. Process., 28, 158–171, https://doi.org/10.1002/ppp.1916, 2017.

Krautblatter, M., Verleysdonk, S., Flores Orozco, A., and Kemna, A.: Temperature – calibrated imaging of seasonal changes in permafrost rock walls by quantitative electrical resistivity tomography (Zugspitze, German/Austrian Alps), J. Geophys. Res., 115, F02003, https://doi.org/10.1029/2008JF001209, 2010.

Krautblatter, M. and Hauck, C.: Electrical resistivity tomography monitoring of permafrost in solid rock walls, J. Geophys. Res.,112, F02S20, doi:10.1029/2006JF000546, 2007.

LaBrecque, D. J., Miletto, M., Daily, W., Ramirez, A., and Owen, E.: The effects of noise on Occam's inversion of resistivity tomography data, Geophysics, 61, 538–548, https://doi.org/10.1190/1.1443980, 1996.

Leroy, P., Revil, A., Kemna, A., Cosenza, P., and Ghorbani, A.: Complex conductivity of water-saturated packs of glass beads, J. Colloid Interface Sci., 321, 103–117, https://doi.org/10.1016/j.jcis.2007.12.031, 2008.

Lesmes, D.P., Frye, K.M.: Influence of pore fluid chemistry on the complex conductivity and induced polarization responses of Berea sandstone, J. Geophys, Res. Solid Earth, 106 (B3), 4079–4090, 2001.

Lesparre, N., Nguyen, F., Kemna, A., Robert, T., Hermans, T., Daoudi, M., and Flores Orozco, A.: A new approach for time-lapse data weighting in electrical resistivity tomography, Geophysics, 82, E325–E333, https://doi.org/10.1190/GEO2017-0024.1, 2017.

Limbrock, J. K. and Kemna, A.: Temperature dependence of SIP ice signatures of partially frozen rocks based on Cole-Cole model parameterization, 6th International Meeting on Induced Polarization, 27– 30 June 2022, p.121-125, https:// doi:10.5281/zenodo.6787016, 2022.

Maierhofer, T., Hauck, C., Hilbich, C., and Flores-Orozco, A.: Spectral Induced Polarization Applied at Different Mountain Permafrost Sites in the European Alps, NSG2021 1st Conference on Hydrogeophysics, European Association of Geoscientists & Engineers, Bordeaux, France, 29 August–2 September 2021, vol. 2021, pp. 1–5, https://doi.org/10.3997/2214-

4609.202120172, 2021.

Maierhofer, T., Hauck, C., Hilbich, C., Kemna, A., and Flores-Orozco, A.: Spectral induced polarization imaging to investigate an ice-rich mountain permafrost site in Switzerland, The Cryosphere, 16, 1903–1925, https://doi.org/10.5194/tc-16-1903-2022, 2022.

Mathys, T., Hilbich, C., Arenson, L. U., Wainstein, P. A., and Hauck, C.: Towards accurate quantification of ice content in permafrost of the Central Andes – Part 2: An upscaling strategy of geophysical measurements to the catchment scale at two study sites, The Cryosphere, 16, 2595–2615, https://doi.org/10.5194/tc-16-2595-2022, 2022.

McKenzie, J. M., Voss, C. I., and Siegel, D. I.: Groundwater flow with energy transport and water-ice phase change: Numerical simulations, benchmarks, and application to freezing in peat bogs, Adv. Water Resour., 30, 966–983, https://doi.org/10.1016/j.advwatres.2006.08.008, 2007.

Mollaret, C., Hilbich, C., Pellet, C., Flores-Orozco, A., Delaloye, R., and Hauck, C.: Mountain permafrost degradation documented through a network of permanent electrical resistivity tomography sites, The Cryosphere, 13, 2557–2578, https://doi.org/10.5194/tc-13-2557-2019, 2019.

Mollaret, C., Wagner, F. M., Hilbich, C., Scapozza, C., and Hauck, C.: Petrophysical Joint Inversion Applied to Alpine Permafrost Field Sites to Image Subsurface Ice, Water, Air, and Rock Contents, Front. Earth Sci., 8, 1–25, https://doi.org/10.3389/feart.2020.00085, 2020.

Mohammed, A.A., B.L. Kurylyk, E.E. Cey, and M. Hayashi.: Snowmelt infiltration and macropore flow in frozen soils: Overview, knowledge gaps, and a conceptual framework, Vadose Zone J., 17:180084, doi:10.2136/vzj2018.04.0084, 2018.

Mudler, J., Hördt, A., Kreith, D., Sugand, M., Bazhin, K., Lebedeva, L., and Radić, T.: Broadband spectral induced polarization for the detection of Permafrost and an approach to ice content estimation – a case study from Yakutia, Russia, The Cryosphere, 16, 4727–4744, https://doi.org/10.5194/tc-16-4727-2022, 2022.

Oldenborger, G. A. and LeBlanc, A. M.: Monitoring changes in unfrozen water content with electrical resistivity surveys in cold continuous permafrost, Geophys. J. Int., 215, 965–977, https://doi.org/10.1093/GJI/GGY321, 2018.

Oldenborger, G. A.: Subzero temperature dependence of electrical conductivity for permafrost geophysics, Cold Regions Science and Technology, 182, 103214, https://doi.org/10.1016/j.coldregions.2020.103214, 2021.

Oldenburg, D. W. and Li, Y.: Estimating depth of investigation in DC resistivity and IP surveys, Geophysics, 64, 403-416 https://doi.org/10.1190/1.1444545, 1999.

Olhoeft, G. R.: Electrical properties of natural clay permafrost, Can. J. Earth Sci., 14, 16–24, 1977.

Parkhomenko, E. I.: Electrical Resistivity of Minerals and Rocks at High Temperature and Pressure, Rev. Geophys. Sp. Phys., 20, 193–218, 1982.

Pogliotti, P., Guglielmin, M., Cremonese, E., Morra di Cella, U., Filippa, G., Pellet, C., and Hauck, C.: Warming permafrost and active layer variability at Cime Bianche, Western European Alps, The Cryosphere, 9, 647–661, https://doi.org/10.5194/tc-9-647-2015, 2015.

Pellet, C., Hilbich, C., Marmy, A., and Hauck, C.: Soil moisture data for the validation of permafrost models using direct and indirect measurement approaches at three alpine sites, Front. Earth Sci., 3, 91, https://doi.org/10.3389/feart.2015.00091, 2016.

N. Pepin, R. S. Bradley, H. F. Diaz, M. Baraer, E. B. Caceres, N. Forsythe, H. Fowler, G. Greenwood, M. Z. Hashmi, X. D. Liu, J. R. Miller, L. Ning, A. Ohmura, E. Palazzi, I. Rangwala, W. Schöner, I. Severskiy, M. Shahgedanova, M. B. Wang, S. N. Williamson & D. Q. Yang: Elevation-dependent warming in mountain regions of the world, Nature Climate Change, 5, 424–430, , 2015.

PERMOS: PERMOS Database, Swiss Permafrost Monitoring Network, Fribourg and Davos, Switzerland [data set], http://www. permos.ch/doi/permos-2021-01.html (last access: 17 May 2022), 2021.

Przyklenk, A., Hördt, A., Radić, T., Capacitively Coupled Resistivity measurements to determine frequency-dependent electrical parameters in periglacial environment—theoretical considerations and first field tests, Geophysical Journal International, Volume 206, Issue 2, August 2016, Pages 1352–1365, https://doi.org/10.1093/gji/ggw178

Rangecroft, S., Suggitt, A. J., Anderson, K., and Harrison, S.: Future climate warming and changes to mountain permafrost in the Bolivian Andes, Climatic Change, 137, 231–243, https://doi.org/10.1007/s10584-016-1655-8, 2016.

Ravanel, L., Magnin, F., and Deline, P.: Impacts of the 2003 and 2015 summer heat waves on permafrost-affected rock-walls in the Mont Blanc massif, Sci. Total Environ., 609, 132–143, https://doi.org/10.1016/j.scitotenv.2017.07.055, 2017.

Revil, A.: Spectral induced polarization of shaly sands: Influence of the electrical double layer, Water Resour. Res., 48, W02517, https://doi.org/10.1029/2011WR011260, 2012.

Revil, A.: Effective conductivity and permittivity of unsaturated porous materials in the frequency range 1 mHz–1 GHz, Water Resour. Res., 49, 306–327, https://doi.org/10.1029/2012WR012700, 2013a.

Revil, A.: On charge accumulation in heterogeneous porous rocks under the influence of an external electric field, Geophysics, 78, 1JA-Z103, https://doi.org/10.1190/geo2012-0503.1, 2013b.

Revil, A. and Glover, P. W. J.: Nature of surface electrical conductivity in natural sands, sandstones, and clays, Geophys. Res. Lett., 25, 691–694, 1998.

Revil, A. and Skold, M.: Salinity dependence of spectral induced polarization in sands and sandstones, Geophys. J. Int., 187, 813– 824, https://doi.org/10.1111/j.1365-246X.2011.05181.x, 2011.

Revil, A., Razdan, M., Julien, S., Coperey, A., Abdulsamad, F., Ghorbani, A., Gasquet, D., Sharma, R., and Rossi, M.: Induced polarization response of porous media with metallic particles – Part 9: Influence of permafrost, Geophysics, 84, E337–E355, https://doi.org/10.1190/geo2019-0013.1, 2019.

Rücker, C., Günther, T., and Wagner, F. M.: pyGIMLi: An open-source library for modelling and inversion in geophysics, Comput. Geosci., 109, 106–123, doi: 10.1016/j.cageo.2017.07.011, 2017.

Schwarz, G.: A theory of the low-frequency dielectric dispersion of colloidal particles in electrolyte solution, J. Phys. Chem., 66, 2636–2642, https://doi.org/10.1021/j100818a067, 1962.

Slater, L., Binley, A. M., Daily, W., and Johnson, R.: Cross-hole electrical imaging of a controlled saline tracer injection, J. Appl. Geophys., 44, 85–102, 2000.

Smith, S., O'Neill, H., Isaksen, K., Noetzli, J., and Romanovsky, V.: The changing thermal state of permafrost, Nat. Rev. Earth Environ., 3, 10–23, https://doi.org/10.1038/s43017-021-00240-1, 2022.

Son, J.-S., Kim, J.-H., and Yi, M.: A new algorithm for SIP parameter estimation from multi-frequency IP data: preliminary

results. A new algorithm for SIP parameter estimation from multifrequency IP data: preliminary results, Explor. Geophys., 38, 60– 68, https://doi.org/10.1071/EG07009, 2007.

Steiner, M., Wagner, F. M., Maierhofer, T., Schöner, W., and Flores Orozco, A.: Improved estimation of ice and water contents in alpine permafrost through constrained petrophysical joint inversion: The Hoher Sonnblick case study, Geophysics, 86, WB119– WB133, https://doi.org/10.1190/geo2020-0592.1, 2021.

Steiner, M., Katona, T., Fellner, J. and Flores Orozco, A.: Quantitative water content estimation in landfills through joint inversion of seismic refraction and electrical resistivity data considering surface conduction, Waste Management, 149, 21–32, https://doi.org/10.1016/j.wasman.2022.05.020, 2022.

Steiner, M., Flores Orozco, A.: formikoj: A flexible library for data management and processing in geophysics—Application for seismic refraction data, Computers and Geosciences, 105339, https://doi.org/10.1016/j.cageo.2023.105339, 2023.

Stillman, D. E., Grimm, R. E., and Dec, S. F.: Low-Frequency Electrical Properties of Ice – Silicate Mixtures, J. Phys. Chem., 114, 6065–6073, https://doi.org/10.1021/jp9070778, 2010.

Supper, R., Ottowitz, D., Jochum, B., Kim, J.-H., Römer, A., Baron, I., Pfeiler, S., Lovisolo, M., Gruber, S., and Vecchiotti, F.: Geoelectrical monitoring: an innovative method to supplement landslide surveillance and early warning, Near Surf. Geophys., 12, 133–150, https://doi.org/10.3997/1873-0604.2013060, 2014.

Vinegar, H. J. and Waxman, M. H.: Induced polarization of shaly sands – the effect of clay counterion type, Geophysics,49, 1267, https://doi.org/10.1190/1.1441755, 1984.

Wagner, F. M., Mollaret, C., Kemna, A., and Hauck, C.: Quantitative imaging of water, ice and air in permafrost systems through petrophysical joint inversion of seismic refraction and electrical resistivity data, Geophys. J. Int., 219, 1866–1875, https://doi.org/10.1093/gji/ggz402, 2019.

Wait, J. R.: Relaxation phenomena and induced polarization, Geoexploration, 22, 107–127, 1984.

Wang, C., Slater L. D, Extending accurate spectral induced polarization measurements into the kHz range: modelling and removal of errors from interactions between the parasitic capacitive coupling and the sample holder, Geophysical Journal International, Volume 218, Issue 2, August 2019, Pages 895–912, https://doi.org/10.1093/gji/ggz199

Ward, S.: The Resistivity And Induced Polarization Methods, in: Conference Proceedings, 1st EEGS Symposium on the Application of Geophysics to Engineering and Environmental Problems Conference, Golden, Colorado, USA, 28–31 March 1988, cp214-00002, European Association of Geoscientists & Engineers, https://doi.org/10.3997/2214-4609-pdb.214.1988_002, 1990.

Waxman, M. H. and Smits, L. J. M.: Electrical conductivities in oilbearing shaly sands, Soc. Pet. Eng. J., 243, 107–122, 1968.

Wu, Q., and T. Zhang, Changes in active layer thickness over the Qinghai-Tibetan Plateau from 1995 to 2007, J. Geophys. Res., 115, D09107, doi:10.1029/2009JD012974, 2010.

Wu, Q., Hubbard S. S.; Ulrich, C. and Wullschleger, S. D., Remote Monitoring of Freeze–Thaw Transitions in Arctic Soils Using the Complex Resistivity Method, Vadose Zone Journal., 12, vzj2012.0062, https://doi.org/10.2136/vzj2012.0062, 2013.

Wu, Y., Nakagawa, S., Kneafsey, T. J., Dafflon, B., and Hubbard, S.: Electrical and seismic response of saline permafrost soil during freeze – Thaw transition, J. Appl. Geophys., 146, 16–26, https://doi.org/10.1016/j.jappgeo.2017.08.008, 2017.

Zhang, T.: Influence of the seasonal snow cover on the ground thermal regime: an overview, Rev. Geophys., 43, RG4002, doi:10.1029/2004RG000157, 2005.

Zimmermann, E., Kemna, A., Berwix, J., Glaas, W., and Vereecken, H.: EIT measurement system with high phase accuracy for the imaging of spectral induced polarization properties of soils and sediments, Meas. Sci. Technol., 19, 094010, https://doi.org/10.1088/0957-0233/19/9/094010, 2008.

Zisser, N., Kemna, A., and Nover, G.: Dependence of spectral – induced polarization response of sandstone on temperature and its relevance to permeability estimation, J. Geophys. Res., 115, B09214, https://doi.org/10.1029/2010JB007526, 2010